



Small-Signal Modeling and Stability Prediction of Parallel Droop-Controlled Inverters Based on Terminal Characteristics of Individual Inverters

Shike Wang , *Student Member, IEEE*, Zeng Liu, *Member, IEEE*, Jinjun Liu , *Fellow, IEEE*, Dushan Boroyevich, *Fellow, IEEE*, and Rolando Burgos, *Member, IEEE*

Abstract—Parallel droop-controlled inverters with renewable energy sources are widely employed in islanded ac microgrids, where dynamic interactions among them may cause small-signal stability issues. Since the active power-frequency droop scheme is applied, the dynamic interactions among inverters exist not only in bus voltage and transmitted current, but also in variable system fundamental frequency. This paper introduces a novel small-signal terminal characteristic model for droop-controlled inverter. Besides conventional impedance and admittance, a new set of terminal characteristics is proposed to characterize the dynamics of fundamental frequency. Furthermore, the small-signal model of parallel inverters is constructed based on the terminal characteristics of individual inverters. Covering the fundamental frequency interactions, a stability prediction approach based on generalized Nyquist criterion is proposed for parallel droop-controlled inverters. Besides the product of impedance and admittance, an additional term is added in the system return ratio, which consists of the proposed terminal characteristics associated with the fundamental frequency. Finally, experimental results validate the effectiveness of this proposed stability prediction approach.

Index Terms—Droop-controlled inverters, fundamental frequency dynamics, stability prediction, terminal characteristics.

I. INTRODUCTION

AS EFFECTIVE solutions of mitigating energy crisis, renewable energy and distributed generation (DG) are now in the cutting edge of development worldwide. With an increasing number of distributed energy resources (DERs) penetrating the utility networks, the concept of microgrid was developed as an integrated system to coordinate and control

the interconnected sources and loads [1], [2]. In islanded ac microgrids, three-phase droop-controlled inverters are widely employed as power interfaces of DGs [3]–[6]. Since the active power-frequency and reactive power-voltage amplitude droop control scheme is applied, automatic power sharing between parallel inverters can be achieved independent of communication [5], [6]. In order to enhance the power sharing accuracy, a virtual impedance control scheme is proposed to improve the performance of a droop-control method [7]. Meanwhile, since all inverters are peer-to-peer, the droop control method has advantages such as plug and play operation, increased power supply reliability, and flexibility in physical location [8]–[10]. When equipped with electric springs, reactive power compensation and demand-side management can be achieved in droop-controlled inverter system [11].

However, although interconnection of the control signal is avoided in parallel droop-controlled inverters, the dynamic interactions between inverters still exist due to the coupling of the system bus. On the basis of the droop scheme, the inverter output active power couples with the fundamental frequency while the reactive power couples with the voltage amplitude, which complicates the stability issues and may jeopardize the operation of overall parallel system [12]. Inspired by the small-signal stability analysis method of the conventional large-scale power system, state-space based approaches are generally employed to analyze the stability of parallel droop-controlled inverters [13]–[16]. The small-signal model of a single inverter is constructed by including the state variables from controllers and power stage. The overall system state matrix can be obtained by combing the small-signal state-space model of each individual inverter, whose eigenvalues reveal the damping of different frequency components and the stability of parallel system. However, the state-space based approaches have inherent limitations. For example, each inverter has 13 state variables in [15], the order of overall system matrix will be multiplied up as the number of paralleled inverters increased. Therefore, it challenges the computation capability. Meanwhile, the inner parameter information of each inverter is required to construct the small-signal state-space model, which is imperative for the stability analysis of a parallel system. In engineering practice of system integration, individual inverters are usually acquired as “black boxes”. In this condition, it is difficult to get access to all inner

Manuscript received September 29, 2018; revised February 8, 2019; accepted April 14, 2019. Date of publication April 30, 2019; date of current version October 18, 2019. This work was supported by the National Natural Science Foundation of China under Grants 51777160 and 51437007. This paper was presented in part at the 8th International Power Electronics and Motion Control Conference, Hefei, China, May 22–26, 2016. Recommended for publication by Associate Editor S. C. Tan. (*Corresponding authors: Zeng Liu and Jinjun Liu.*)

S. Wang, Z. Liu, and J. Liu are with the State Key Lab of Electrical Insulation and Power Equipment, School of Electrical Engineering, Xi’an Jiaotong University, Xi’an 710049, China (e-mail: wangshikepe@gmail.com; zengliu@mail.xjtu.edu.cn; jjliu@mail.xjtu.edu.cn).

D. Boroyevich and R. Burgos are with the Center for Power Electronics Systems, Bradley Department of Electrical and Computer Engineering, Virginia Polytechnic Institute and State University, Blacksburg, VA 24061 USA (e-mail: dushan@vt.edu; rolando@vt.edu).

Color versions of one or more of the figures in this paper are available online at <http://ieeexplore.ieee.org>.

Digital Object Identifier 10.1109/TPEL.2019.2914176

information of each inverter. Therefore, the state-space based stability analysis approaches lack practicability in real application.

The impedance-based approaches have been proposed for modeling and stability analysis of three-phase ac power electronic systems [17]–[20]. Comparing with the state matrix in state-space based approach, small-signal impedance and admittance are applied to represent the terminal dynamics of power converters, simplifying the computation process. Furthermore, the impedance-based approaches do not rely on the inner parameter information and analytical model of power converters. The terminal impedance and admittance can be directly obtained by external measurement [21]–[23], which makes this method more practical. It is widely applied to study the grid-connected three-phase converters [24]–[26], cascaded voltage source inverter and constant power loads [27], [28], as well as parallel inverters with an active load sharing scheme [29].

As for the parallel droop-controlled inverters, relevant works on impedance-based modeling and stability analysis have been presented [30]–[32]. In [30], the droop-controlled inverter is modeled as a two-terminal Thévenin equivalent circuit of a controlled voltage source in series with an output impedance. A transfer function covering dynamic behaviors of the voltage control loop and LC filter is derived as the inverter output impedance. This impedance model is then adopted in [31] to analyze the stability of parallel droop-controlled and PQ-controlled inverters. By representing droop-controlled inverters as Thévenin circuits, whereas PQ-controlled inverters as Norton circuits, the model of overall system is derived as a double closed-loop system. On the basis of Nyquist criterion, the impact of distribution cable impedance and the penetration of PQ-controlled inverters on the system stability are analyzed. However, since the power loop and droop scheme are neglected in this impedance model [30], it is inaccurate to reflect the complete small-signal dynamics of the droop-controlled inverter, and the impacts of critical parameters such as droop slopes on stability cannot be analyzed. Covering the complete control scheme and power stage, an analytical small-signal impedance model of a single droop-controlled inverter is proposed in [32]. Although the dynamics of power droop control is considered, only a single inverter operating in the islanded mode is studied. The principle to utilize this impedance model in modeling and stability analysis of parallel droop-controlled inverters is not discussed. Since no further studies are developed, the generalized Nyquist criterion (GNC) [19], [20] based small-signal stability prediction for parallel droop-controlled inverters is obstructed.

Focusing on the small-signal stability issues related to dynamic interactions among parallel droop-controlled inverters, this paper presents a stability prediction approach based on the terminal characteristics of individual inverters, and its contribution can be highlighted below. At the beginning, this paper introduces a novel set of small-signal terminal characteristics for a droop-controlled inverter. Based on the droop scheme, the fundamental frequency always varies with the inverter output active power [5], [6]. In an islanded parallel system, the dynamic interactions between inverters exist not only in bus voltage and transmitted current, but

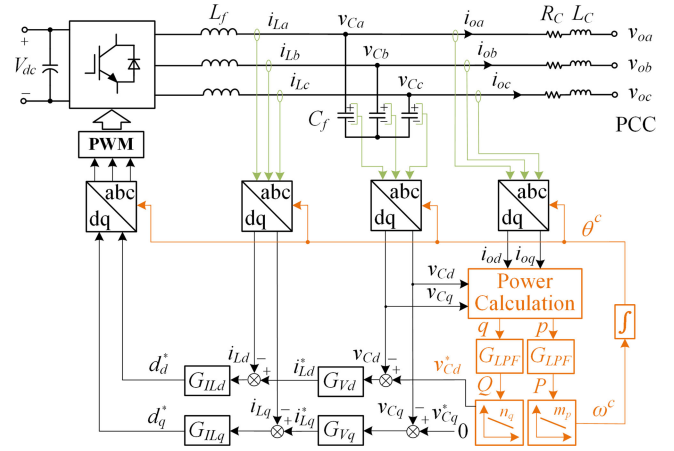


Fig. 1. Block diagram of a typical three-phase droop-controlled inverter.

also in variable system fundamental frequency. Therefore, the comprehensive terminal characteristics of a droop-controlled inverter also involve the fundamental frequency dynamics. Besides conventional impedance and admittance, a new set of terminal characteristics is proposed to represent the interactions between small-signal dynamics of inverter terminal current and fundamental frequency. Furthermore, the small-signal model of parallel droop-controlled inverters is constructed. Based on GNC, a stability prediction approach is proposed. Besides the product of impedance and admittance, the proposed new terminal characteristics are added in the system return ratio to cover the fundamental frequency interactions between parallel inverters. Finally, the measurement procedures of inverter terminal characteristics are presented. Since the measured results intrinsically model all control scheme and circuit components [21]–[23], the stability of parallel droop-controlled inverters can be readily predicted using the proposed approach, independent of the analytical small-signal model of individual inverters.

The rest of this paper includes five sections. Section II introduces the small-signal terminal characteristics of a single droop-controlled inverter. Section III proposes a modeling and stability prediction approach for parallel droop-controlled inverters. Section IV presents the terminal characteristic measurement results, based on which the small-signal stability of parallel inverters is predicted using the proposed approach in Section V. Experimental results are presented in Section VI. Section VII remarks the conclusion.

II. TERMINAL CHARACTERISTICS OF INDIVIDUAL DROOP-CONTROLLED INVERTER

A. Description of Studied Droop-Controlled Inverter

The power stage and the control block diagram of a typical three-phase droop-controlled inverter are depicted in Fig. 1 [5], [6]. In the power stage, the DERs usually feed in dc side to provide electric energy. The dc bus voltage is generally controlled to be stable. Thus, the dynamic from dc input is neglected. The LC filter is adopted in ac side to filter the switching ripples, where filter capacitors with low equivalent series resistance (ESR)

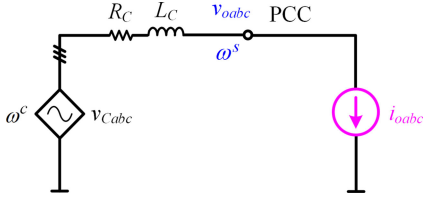


Fig. 2. Operation configuration of voltage representation.

are generally used. Therefore, the ESR of filter capacitors is neglected. The output terminal of the LC filter is tied to the point of common coupling (PCC) through a distribution cable with the resistance R_C and inductance L_C . As shown in Fig. 1, the external power loop functions the droop control scheme. The instantaneous output active and reactive powers are calculated as

$$p = \frac{3}{2}(v_{Cd}i_{od} + v_{Cq}i_{oq}), \quad q = \frac{3}{2}(-v_{Cd}i_{oq} + v_{Cq}i_{od}). \quad (1)$$

The low-pass filter (LPF) is applied to obtain the fundamental component P and Q in (2). ω_f is the cutoff frequency of power LPF

$$P = G_{LPF}p, \quad Q = G_{LPF}q$$

$$G_{LPF} = \frac{\omega_f}{s + \omega_f}. \quad (2)$$

The references of the fundamental frequency and capacitor voltage amplitude are regulated to vary with the output active and reactive powers based on the droop scheme

$$\omega^c = \omega_0 - m_p(P - P_0), \quad v_{Cd}^* = V_0 - n_q(Q - Q_0) \quad (3)$$

where m_p and n_q are active and reactive power droop slopes, $m_p, n_q > 0$. P_0 and Q_0 are initial output power setting points at the rated fundamental frequency ω_0 and voltage amplitude V_0 .

The internal voltage loop regulates the capacitor voltage to track the references. Besides, an inductor current loop is usually adopted for damping the resonance of the LC filter and improving the dynamic performance. Under the regulation of both power loop and voltage loop, the droop-controlled inverter can be regarded as a controlled voltage source with the capability of power limitation. When working in the standalone mode and defining the PCC voltage, the internal voltage loop is dominant. Once the fundamental frequency and amplitude of the PCC voltage are already defined by other paralleled voltage source, the inverter output current can always be regulated by the external power loop. Therefore, a single droop-controlled inverter can be represented in both voltage and current operation modes, where its terminal characteristics are defined separately.

B. Voltage Representation

The voltage representation is defined for the islanded operation mode of droop-controlled inverter. As shown in Fig. 2, the fundamental frequency ω^c and the amplitude of inverter output voltage on filter capacitor v_{Cabc} are regulated to follow the references in (3). Since there is no other voltage source connected to

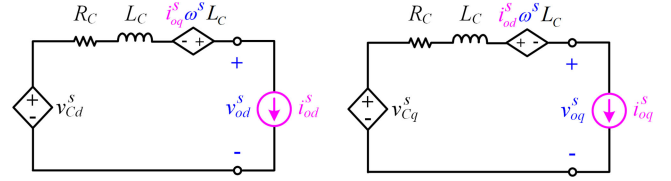
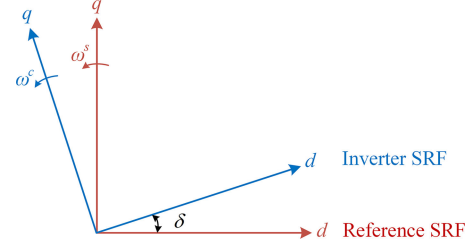
Fig. 3. Equivalent circuits of voltage representation in dq -frame.

Fig. 4. Diagram of inverter individual SRF and reference SRF.

PCC, the PCC voltage v_{oabc} is defined by v_{Cabc} , which equals to the subtraction of a voltage drop on the distribution cable from v_{Cabc} . The fundamental frequency of the PCC voltage ω^s is equal to ω^c . The loads connected to PCC determine the inverter output current i_{oabc} . Since only the terminal dynamics of the droop-controlled inverter are focused, the dynamics of loads are excluded. The external load connected to PCC is regarded as an ideal current sink.

The equivalent circuit of Fig. 2 in the dq -frame is derived in Fig. 3. Since all circuit variables must be transformed in a common synchronous reference frame (SRF), this reference SRF is chosen to be aligned to the PCC voltage. The variables in Fig. 3 are all represented in the common reference SRF marked by superscript s .

Based on Fig. 3, the equation between \mathbf{v}_{Cdq}^s , \mathbf{i}_{odq}^s , \mathbf{v}_{odq}^s and ω^s can be expressed as

$$v_{od}^s = v_{Cd}^s - i_{od}^s \cdot (sL_C + R_C) + i_{oq}^s \cdot \omega^s L_C$$

$$v_{oq}^s = v_{Cq}^s - i_{oq}^s \cdot (sL_C + R_C) - i_{od}^s \cdot \omega^s L_C. \quad (4)$$

According to Fig. 1, the capacitor voltage is regulated by external power droop control, internal voltage, and current control loops. The control schemes are implemented in the inverter individual SRF aligned to the capacitor voltage, which is marked by superscript c . However, the circuit variables in Fig. 3 are represented in the common reference SRF aligned to the PCC voltage. In order to study the overall interaction mechanism, it is necessary to conduct the transformation of the capacitor voltage and output current in different SRFs.

In Fig. 4, the phase angle difference δ between two SRFs can be calculated as

$$\delta = \delta_0 + \int (\omega^c - \omega^s) dt \quad \hat{\delta} = \int (\hat{\omega}^c - \hat{\omega}^s) dt \quad (5)$$

where δ_0 represents the steady-state phase angle difference between the capacitor voltage and PCC voltage.

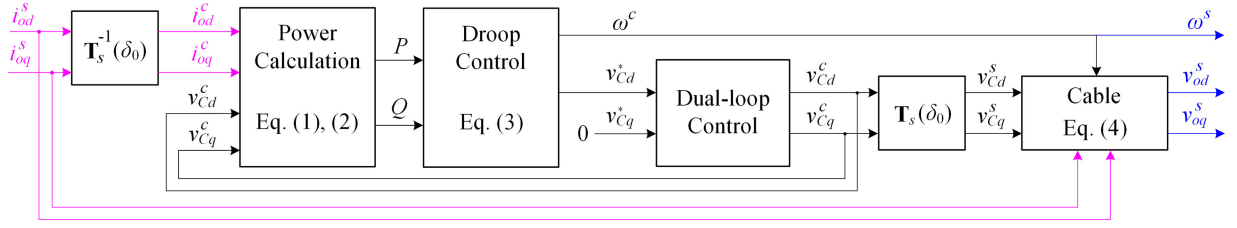


Fig. 5. Interaction mechanism of voltage representation.

The transformation matrix of the capacitor voltage and output current in different SRFs can be expressed by

$$\begin{aligned} \mathbf{v}_{Cdq}^s &= \mathbf{T}_s(\delta) \cdot \mathbf{v}_{Cdq}^c & \mathbf{v}_{Cdq}^c &= \mathbf{T}_s^{-1}(\delta) \cdot \mathbf{v}_{Cdq}^s \\ \mathbf{i}_{odq}^s &= \mathbf{T}_s(\delta) \cdot \mathbf{i}_{odq}^c & \mathbf{i}_{odq}^c &= \mathbf{T}_s^{-1}(\delta) \cdot \mathbf{i}_{odq}^s \end{aligned} \quad (6)$$

where

$$\mathbf{T}_s(\delta) = \begin{bmatrix} \cos(\delta) & -\sin(\delta) \\ \sin(\delta) & \cos(\delta) \end{bmatrix}.$$

Since PCC voltage is defined by inverter capacitor voltage in islanded mode, ω^s and ω^c are always identical. Therefore, the dynamic of δ can be neglected in voltage representation, $\delta \equiv \delta_0$.

Based on (1) to (6), the overall interaction mechanism of droop-controlled inverter in voltage representation can be depicted in Fig. 5. In Fig. 5, the inverter output current \mathbf{i}_{odq}^s is regarded as an input excitation. The fundamental frequency ω^s and dq -amplitude \mathbf{v}_{odq}^s of the PCC voltage are output responses. If there exists small-signal disturbance of \mathbf{i}_{odq}^s , through the power droop control, capacitor voltage and inductor current dual-loop control, and distribution cable, it will generate small-signal dynamics of ω^s and \mathbf{v}_{odq}^s . Therefore, the terminal characteristics of a droop-controlled inverter in voltage representation can be defined as shown in Fig. 6. The output impedance \mathbf{Z}_{odq} describes the relationship between the small-signal dynamics of PCC voltage amplitude and output current, which has the same physical meaning as the conventional small-signal output impedance in existing literatures [21]–[29]. A new terminal characteristic $\mathbf{G}_{\omega i}$ is proposed to characterize the dynamic interaction from the excitation of output current to its response of the fundamental frequency. As ω^s is a scalar with a single dimension, $\mathbf{G}_{\omega i}$ is a 1×2 matrix as (7) shows. Since the conventional definition of output impedance and admittance requires the direction of current to be input [21]–[29], there exists a minus in Fig. 6

$$\begin{aligned} \mathbf{Z}_{odq} &= \begin{bmatrix} Z_{odd} & Z_{odq} \\ Z_{oqd} & Z_{oqq} \end{bmatrix} \\ \mathbf{G}_{\omega i} &= [G_{\omega id} \quad G_{\omega iq}]. \end{aligned} \quad (7)$$

C. Current Representation

As shown in Fig. 7, the droop-controlled inverter is connected with other voltage source that has already defined the voltage v_{oabc} and fundamental frequency ω^s at PCC. In this case, the droop-controlled inverter is represented in the current operation mode. The inverter output power, i.e., output current i_{oabc} is determined by the amplitude and phase angle differences between

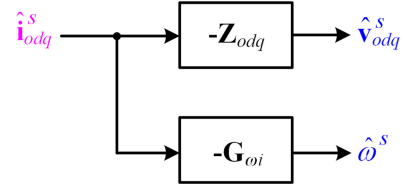


Fig. 6. Definition of small-signal terminal characteristics of voltage representation.

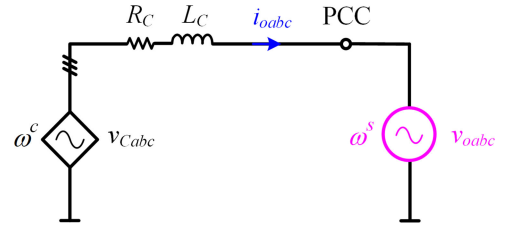


Fig. 7. Operation configuration of current representation.

capacitor voltage v_{Cabc} and PCC voltage v_{oabc} . Since v_{oabc} and ω^s are set by external voltage source, the inverter output current i_{oabc} can be regulated by changing the fundamental frequency ω^c and amplitude of v_{Cabc} based on the droop scheme in (3).

The equivalent circuit of Fig. 7 in the dq -frame is derived in Fig. 8. Similar to Fig. 3, the reference SRF in Fig. 8 is also chosen to be aligned to PCC voltage, which is marked by superscript s .

Based on Fig. 8, the equation between \mathbf{v}_{Cdq}^s , \mathbf{i}_{odq}^s , \mathbf{v}_{odq}^s , and ω^s can be expressed as

$$\begin{aligned} i_{od}^s &= \frac{[(sLC + RC) \cdot (v_{Cd}^s - v_{od}^s) + \omega^s LC \cdot (v_{Cq}^s - v_{oq}^s)]}{[(sLC + RC)^2 + (\omega^s LC)^2]} \\ i_{oq}^s &= \frac{[(sLC + RC) \cdot (v_{Cq}^s - v_{oq}^s) - \omega^s LC \cdot (v_{Cd}^s - v_{od}^s)]}{[(sLC + RC)^2 + (\omega^s LC)^2]}. \end{aligned} \quad (8)$$

As mentioned earlier, the capacitor voltage is regulated by inner control schemes implemented in the inverter individual SRF. Therefore, the phase angle difference δ between the inverter individual SRF and reference SRF can still be calculated as (5). Different with voltage representation, in the current operation mode, since the PCC voltage is independent of the inverter capacitor voltage, their fundamental frequency ω^s and ω^c are two irrelevant variables. The integral term in (5) cannot be neglected, which reflects the dynamic of δ .

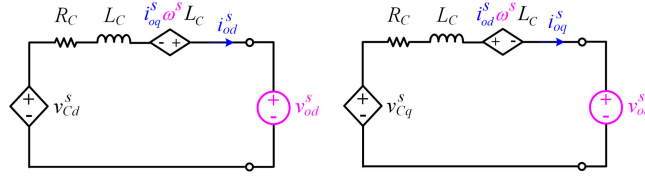
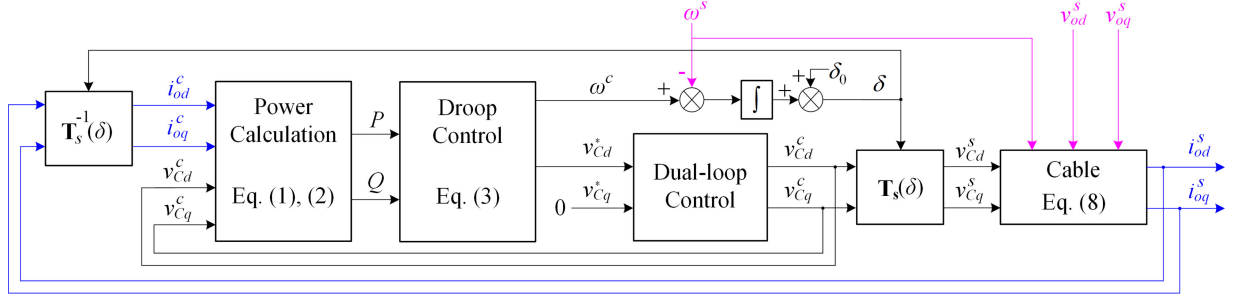
Fig. 8. Equivalent circuits of current representation in dq -frame.

Fig. 9. Interaction mechanism of current representation.

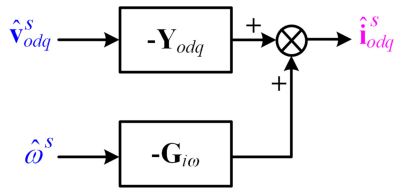


Fig. 10. Definition of small-signal terminal characteristics of current representation.

On the basis of (1) to (3), (5) to (6), and (8), the overall interaction mechanism of a droop-controlled inverter in current representation can be depicted in Fig. 9. In Fig. 9, fundamental frequency ω^s and dq -amplitude \mathbf{v}_{odq}^s of the PCC voltage are regarded as external input excitations while inverter output current $\hat{\mathbf{i}}_{odq}^s$ is the output response. For a certain steady-state operating point, if there exist small-signal disturbances of ω^s and \mathbf{v}_{odq}^s , according to (8), they will generate $\hat{\mathbf{i}}_{odq}^s$. After being transformed to the inverter individual SRF, $\hat{\mathbf{i}}_{odq}^c$ will generate the small-signal dynamics of ω^c and \mathbf{v}_{Cdq}^c through the power droop control and inner dual-loop control. Then, the small-signal variation of capacitor voltage further changes $\hat{\mathbf{i}}_{odq}^s$ based on (8). Along with the external disturbance from the fundamental frequency of PCC voltage ω^s , the small-signal dynamic of the fundamental frequency of inverter individual SRF ω^c influences the dynamic of phase angle difference δ as (5) shows. According to (6), there will also exist dynamic interactions in the transformation of circuit variables between different SRFs. Based on Fig. 9, the terminal characteristics of droop-controlled inverter in current representation can be defined as shown in Fig. 10. The output admittance \mathbf{Y}_{odq} represents the relationship between the small-signal dynamics of the inverter output current and PCC voltage amplitude, which has the same physical meaning as the conventional output admittance in existing literatures [21]–[29].

The $\mathbf{G}_{i\omega}$ is a newly proposed terminal characteristic, which describes the small-signal dynamic interaction between inverter output current and fundamental frequency of the PCC voltage. The expressions of \mathbf{Y}_{odq} and $\mathbf{G}_{i\omega}$ are shown in (9). Due to the direction of current is output, similar to \mathbf{Z}_{odq} and $\mathbf{G}_{\omega i}$, there also exists a minus in the definition of \mathbf{Y}_{odq} and $\mathbf{G}_{i\omega}$.

$$\mathbf{Y}_{odq} = \begin{bmatrix} Y_{odd} & Y_{odq} \\ Y_{oqd} & Y_{oqq} \end{bmatrix}$$

$$\mathbf{G}_{i\omega} = \begin{bmatrix} G_{id\omega} \\ G_{iq\omega} \end{bmatrix}. \quad (9)$$

III. MODELING AND STABILITY PREDICTION FOR PARALLEL DROOP-CONTROLLED INVERTERS

A. System Description

The typical configuration of N parallel droop-controlled inverters is shown in Fig. 11. Inverters are connected to system ac bus through the distribution cable Z_C . Since only the dynamics of inverters are considered, the external load connected to PCC is assumed to be an ideal current sink. In islanded ac microgrids, parallel inverters in Fig. 11 are required to supply a stable PCC voltage. Since the fundamental frequency and output voltage amplitude of each inverter are dynamically regulated with their output active and reactive powers based on the droop scheme in (3), the amplitude and fundamental frequency of PCC voltage also vary with the total output power, i.e., total output current. Therefore, the overall parallel inverters can be equivalent to one controlled voltage source whose small-signal terminal characteristics are described in the voltage representation as Fig. 12 shows. The total output current is regarded as the input excitation while the fundamental frequency ω^s and dq -amplitude

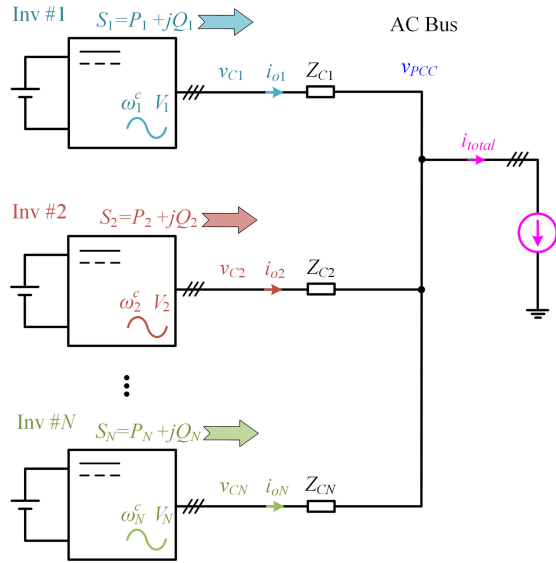


Fig. 11. Typical configuration of parallel droop-controlled inverters.

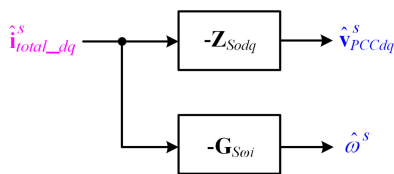


Fig. 12. Definition of equivalent small-signal terminal characteristics of parallel droop-controlled inverters.

of PCC voltage are regarded as the output responses. The output impedance \mathbf{Z}_{Sodq} and fundamental frequency-output current terminal characteristic $\mathbf{G}_{S\omega i}$ represent the dynamic interactions between total output current and PCC voltage in small-signal sense, including amplitude and fundamental frequency. In order to study the small-signal stability of parallel inverters, the relationship between overall terminal characteristics \mathbf{Z}_{Sodq} , $\mathbf{G}_{S\omega i}$ and those of individual inverters must be obtained. Since the direction of total current is output, there is a minus in the definition of \mathbf{Z}_{Sodq} and $\mathbf{G}_{S\omega i}$.

B. System Modeling

As discussed in Section II, the small-signal terminal characteristics of a single droop-controlled inverter can be described in either voltage or current representation, depending on the type of external connected perturbation source. In Fig. 11, for every single inverter, other $N-1$ inverters can be regarded as perturbation sources. On the one hand, $i_{total} = \sum_{k=1}^N i_{ok}$, if the total current is assumed to equal to a certain value, the output current of Inv # k ($k = 1, 2, \dots, N$) i_{ok} is determined by $i_{o1}, i_{o2}, \dots, i_{ok-1}, i_{ok+1}, \dots, i_{oN}$. The ω_k^s and V_k are dynamically regulated with i_{ok} , whose terminal characteristics can be described as the voltage representation. On the other hand, $v_{PCC} = v_{C1} - i_{o1}Z_{C1} = v_{C2} - i_{o2}Z_{C2} = \dots = v_{CN} - i_{oN}Z_{CN}$, PCC voltage is the result of synchronization and power sharing between all parallel inverters, including its amplitude and fundamental frequency. For

each single inverter, it is equivalent to be connected with a virtual controlled voltage source v_{PCC} . In this case, the inverter terminal characteristics should be represented in the current representation. Therefore, when operating in a parallel system, the features of a droop-controlled inverter in both two representations are expressed simultaneously. However, in order to characterize the interaction mechanism between parallel droop-controlled inverters and built the small-signal model to predict stability, each inverter should be described only in one certain representation. Since the fundamental frequency and amplitude of PCC voltage should be uniquely identified, all parallel inverters can be classified into two groups. As shown in the small-signal block diagram in Fig. 13, the first group is composed of a single inverter with the terminal characteristics described in voltage representation. This inverter defines the small-signal dynamics of voltage amplitude \hat{v}_{PCCdq}^s and fundamental frequency $\hat{\omega}^s$ at PCC. The rest $N-1$ inverters belong to the second group, which are described in current representation. Together with the total output current $\hat{i}_{total_dq}^s$, the output current of inverters from the second group $\hat{i}_{odq2}^s \cdots \hat{i}_{odqN}^s$ decides the value of \hat{i}_{odq1}^s , and further influences \hat{v}_{PCCdq}^s and $\hat{\omega}^s$. Meanwhile, \hat{v}_{PCCdq}^s and $\hat{\omega}^s$ also perturb the output current of inverters from the second group. After partitioning the parallel inverters under this structure, the interaction loops of not only voltage and current, but also fundamental frequency and current are described. Since the role of each parallel inverter is peer to peer, any inverter can be chosen as the first group, which is equivalent for stability prediction of the parallel system.

Based on Figs. 12 and 13, the expressions of overall terminal characteristics \mathbf{Z}_{Sodq} and $\mathbf{G}_{S\omega i}$ can be derived as

$$\begin{aligned} \mathbf{Z}_{Sodq} &= \mathbf{Z}_{odq1} \cdot \left(\mathbf{I} + \sum_{k=2}^N \mathbf{Y}_{odqk} \cdot \mathbf{Z}_{odq1} + \sum_{k=2}^N \mathbf{G}_{i\omega k} \cdot \mathbf{G}_{\omega i1} \right)^{-1} \\ \mathbf{G}_{S\omega i} &= \mathbf{G}_{\omega i1} \cdot \left(\mathbf{I} + \sum_{k=2}^N \mathbf{Y}_{odqk} \cdot \mathbf{Z}_{odq1} + \sum_{k=2}^N \mathbf{G}_{i\omega k} \cdot \mathbf{G}_{\omega i1} \right)^{-1} \end{aligned} \quad (10)$$

where \mathbf{I} is the two-dimension unit matrix.

C. Stability Prediction Approach

According to (10), Fig. 13 can be transformed to Fig. 14, where \mathbf{Z}_{Sodq} and $\mathbf{G}_{S\omega i}$ are equivalent to the series of a feedback loop and corresponding terminal characteristics of the inverter modeled in voltage representation. Since the direction of the total output current is output in Fig. 14, there is a minus before $\hat{i}_{total_dq}^s$.

The stability prediction of a parallel system should be conducted on the premise that each single inverter operates stably. Therefore, there is no right-half-plane (RHP) pole in terminal characteristics of an individual inverter, \mathbf{Z}_{odq1} , $\mathbf{G}_{\omega i1}$ and \mathbf{Y}_{odqk} , $\mathbf{G}_{i\omega k}$, $k = 2, \dots, N$. According to (10) and Fig. 14, the overall system stability is just determined by the feedback loop. According to GNC [19], [20], the system return ratio \mathbf{L} is

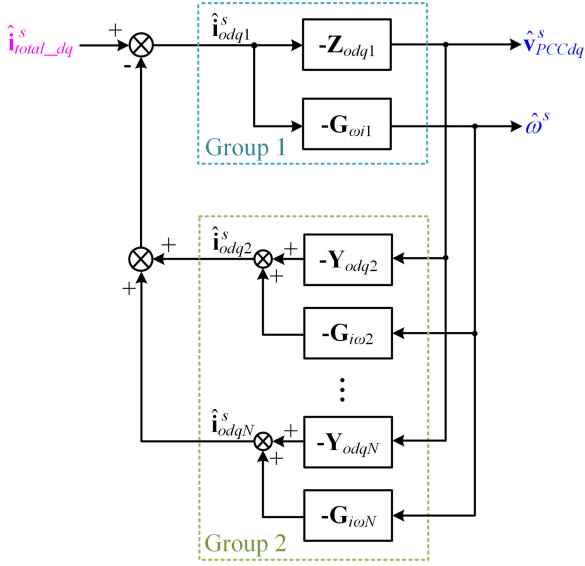


Fig. 13. Small-signal block diagram of parallel inverters.

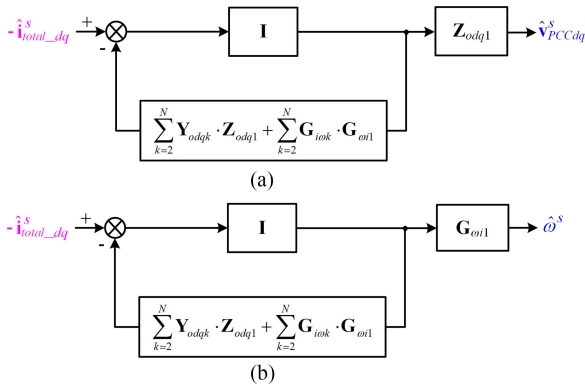


Fig. 14. Equivalent small-signal block diagram of parallel inverters for applying GNC.

defined as (11)

$$\mathbf{L} = \sum_{k=2}^N \mathbf{Y}_{odqk} \cdot \mathbf{Z}_{odq1} + \sum_{k=2}^N \mathbf{G}_{i\omega k} \cdot \mathbf{G}_{\omega i1}. \quad (11)$$

The number of RHP pole Z in \mathbf{Z}_{Sodq} and $\mathbf{G}_{S\omega i}$ can be obtained

$$Z = -N_L \quad (12)$$

where N_L denotes the net sum of anticlockwise encirclements of the critical point $(-1 + j0)$ by the characteristic loci of \mathbf{L} . Consequently, it can be stated that the parallel droop-controlled inverter system is stable if and only if the characteristic loci of return ratio \mathbf{L} do not encircle the critical point $(-1 + j0)$.

In summary, based on the proposed stability prediction approach expressed by (11) and (12), the stability of parallel droop-controlled inverters can be accessed by the terminal characteristics of each individual inverter. The terminal characteristics of a single inverter can be readily obtained by external

measurement, where the inner parameters and analytical model are not required.

IV. SIMULATION VERIFICATION OF SYSTEM MODEL

In this section, the terminal characteristic measurement principle of single inverter is discussed first. Second, the simulation measurement results based on SABER is presented. In order to verify the proposed small-signal model, not only the terminal characteristics of individual inverters, but also those of parallel inverters are measured in simulation.

A. Terminal Characteristic Measurement Principle

In order to measure the terminal characteristics, small perturbations are injected into the inverter. The pertinent response signals are processed and calculated to obtain the amplitude ratio and phase difference between the perturbation and response signals over the frequency range of interest. Based on different types of measured terminal characteristics, the shunt current injection and series voltage injection methods are applied [21]–[23], which are discussed, respectively, for voltage and current representations.

According to the terminal characteristic definition of voltage representation in Fig. 6 and equation (7), the perturbation signal is output current while the response signals are the dq -voltage amplitude and fundamental frequency. In steady state, the droop-controlled inverter is connected to an ideal current sink. In order to measure \mathbf{Z}_{odq} and $\mathbf{G}_{\omega i}$, a shunt current perturbation should be injected to the terminal of droop-controlled inverter, which is illustrated in Fig. 15. According to previous research in [21], the suppressed-carrier injection technique is applied. With this method, the dq -current perturbation signals i_{pd} , i_{pq} are generated by the network analyzer as

$$\begin{aligned} i_{pd} &= I_P \cos(\omega_{ip} t) \cos(\phi_{ip}) \\ i_{pq} &= I_P \cos(\omega_{ip} t) \sin(\phi_{ip}) \end{aligned} \quad (13)$$

where I_P is the current injection amplitude. ϕ_{ip} is the current injection angle. ω_{ip} is the current injection radian frequency, which will be swept over a range of interest. The three-phase injected current perturbation i_{pabc} is obtained as

$$\begin{aligned} i_{pa} &= I_P \cos(\omega_{ip} t) \cos(\theta^s + \phi_{ip}) \\ i_{pb} &= I_P \cos(\omega_{ip} t) \cos\left(\theta^s - \frac{2}{3}\pi + \phi_{ip}\right) \\ i_{pc} &= I_P \cos(\omega_{ip} t) \cos\left(\theta^s + \frac{2}{3}\pi + \phi_{ip}\right). \end{aligned} \quad (14)$$

An SRF phase-locked loop (PLL) is adopted to acquire the phase of PCC voltage θ^s to implement the coordinate transformation [33]. Meanwhile, as the response signal of $\mathbf{G}_{\omega i}$, the fundamental frequency of PCC voltage ω^s is also measured by SRF-PLL. In (7), the \mathbf{Z}_{odq} matrix consists of four elements. Therefore, at least two independent perturbations should be injected at a certain frequency point ω_{ip} to solve the linear equation as shown in (15), where the subscripts 1 and 2 denote the first and the second perturbation injections. According to (7), there are

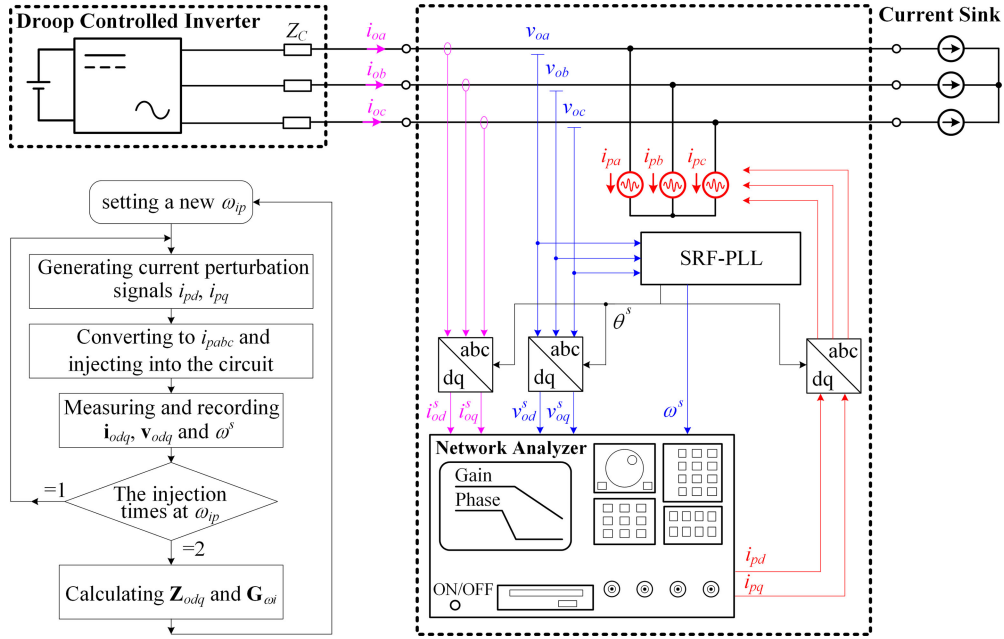


Fig. 15. Block diagram of shunt current injection measurement for voltage representation.

another two elements in the newly proposed frequency-output current terminal characteristic $\mathbf{G}_{\omega i}$. Since $\mathbf{G}_{\omega i}$ and \mathbf{Z}_{odq} share the same input perturbation signal $\hat{\mathbf{i}}_{odq}$, no additional injection is required. Likewise, the value of two elements in $\mathbf{G}_{\omega i}$ can be measured simultaneously as (16). Since the direction of perturbation current in Fig. 15 is output, there exists a minus in (15) and (16). The flow chart in Fig. 15 illustrates the overall procedures of measuring \mathbf{Z}_{odq} and $\mathbf{G}_{\omega i}$ with the frequency sweep approach

$$\mathbf{Z}_{odq}(\omega_{ip}) = \begin{bmatrix} Z_{odd}(\omega_{ip}) & Z_{odq}(\omega_{ip}) \\ Z_{oqd}(\omega_{ip}) & Z_{oqq}(\omega_{ip}) \end{bmatrix} = - \begin{bmatrix} v_{od1}^s(\omega_{ip}) & v_{od2}^s(\omega_{ip}) \\ v_{oq1}^s(\omega_{ip}) & v_{oq2}^s(\omega_{ip}) \end{bmatrix} \cdot \begin{bmatrix} i_{od1}^s(\omega_{ip}) & i_{od2}^s(\omega_{ip}) \\ i_{oq1}^s(\omega_{ip}) & i_{oq2}^s(\omega_{ip}) \end{bmatrix}^{-1} \quad (15)$$

$$\mathbf{G}_{\omega i}(\omega_{ip}) = \begin{bmatrix} G_{wid}(\omega_{ip}) & G_{wiq}(\omega_{ip}) \end{bmatrix} = - \begin{bmatrix} \omega_1^s(\omega_{ip}) & \omega_2^s(\omega_{ip}) \end{bmatrix} \cdot \begin{bmatrix} i_{od1}^s(\omega_{ip}) & i_{od2}^s(\omega_{ip}) \\ i_{oq1}^s(\omega_{ip}) & i_{oq2}^s(\omega_{ip}) \end{bmatrix}^{-1} \quad (16)$$

According to the terminal characteristic definition of current representation in Fig. 10 and (9), a series voltage perturbation should be injected to the terminal of a droop-controlled inverter, which is illustrated in Fig. 16. When operating in the current representation, the droop-controlled inverter is series connected

to a controlled voltage source with rated voltage amplitude V_R and rated fundamental frequency ω_R .

The mechanism of generating dq -voltage amplitude perturbation is similar to that of generating dq -current perturbation in (13). The dq -voltage perturbation signals v_{pd} , v_{pq} are generated by the network analyzer as

$$\begin{aligned} v_{pd} &= V_P \cos(\omega_{vp}t) \cos(\phi_{vp}) \\ v_{pq} &= V_P \cos(\omega_{vp}t) \sin(\phi_{vp}) \end{aligned} \quad (17)$$

where V_P is the voltage injection amplitude. ϕ_{vp} is the voltage injection angle. ω_{vp} is the voltage injection radian frequency.

As shown in Fig. 16, after adding v_{pd} , v_{pq} to the rated dq -voltage amplitude and converting to abc -frame, the three-phase output instruction for controlled voltage source is obtained as v_{pabc}

$$\begin{aligned} v_{pa} &= V_P \cos(\omega_{vp}t) \cos(\omega_R t + \phi_{vp}) + V_R \cos(\omega_R t) \\ v_{pb} &= V_P \cos(\omega_{vp}t) \cos\left(\omega_R t - \frac{2}{3}\pi + \phi_{vp}\right) \\ &\quad + V_R \cos\left(\omega_R t - \frac{2}{3}\pi\right) \\ v_{pc} &= V_P \cos(\omega_{vp}t) \cos\left(\omega_R t + \frac{2}{3}\pi + \phi_{vp}\right) \\ &\quad + V_R \cos\left(\omega_R t + \frac{2}{3}\pi\right). \end{aligned} \quad (18)$$

Since the output admittance \mathbf{Y}_{odq} in (9) represents the dynamic interaction from the excitation of dq -voltage amplitude

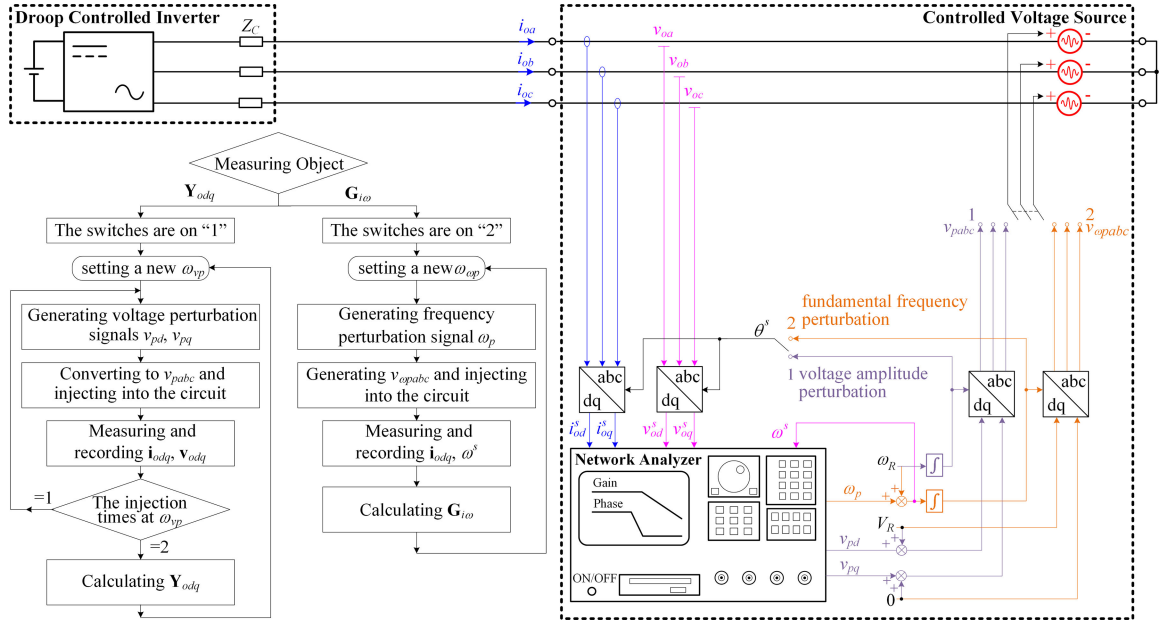


Fig. 16. Block diagram of series voltage injection measurement for current representation.

to its response of output current, it can be measured as

$$\begin{aligned} \mathbf{Y}_{odq}(\omega_{vp}) &= \begin{bmatrix} Y_{odd}(\omega_{vp}) & Y_{odq}(\omega_{vp}) \\ Y_{oqd}(\omega_{vp}) & Y_{oqq}(\omega_{vp}) \end{bmatrix} \\ &= - \begin{bmatrix} i_{od1}^s(\omega_{vp}) & i_{od2}^s(\omega_{vp}) \\ i_{oq1}^s(\omega_{vp}) & i_{oq2}^s(\omega_{vp}) \end{bmatrix} \\ &\quad \cdot \begin{bmatrix} v_{od1}^s(\omega_{vp}) & v_{od2}^s(\omega_{vp}) \\ v_{oq1}^s(\omega_{vp}) & v_{oq2}^s(\omega_{vp}) \end{bmatrix}^{-1} \end{aligned} \quad (19)$$

where the subscripts 1 and 2 denote two linearly independent injections at a certain frequency point ω_{vp} .

In order to measure the proposed output current-frequency terminal characteristic $\mathbf{G}_{i\omega}$, small perturbation signal ω_p is injected to the fundamental frequency of the PCC voltage. As Fig. 16 shows, the three-phase voltage instruction with perturbed fundamental frequency $v_{\omega p abc}$ is expressed as (20). It indicates that perturbing the fundamental frequency of PCC voltage is equivalent to adding a perturbation signal to its phase angle

$$\begin{aligned} \omega_p &= \Omega_P \cos(\omega_{\omega p} \tau) \\ v_{\omega pa} &= V_R \cos \left(\int_0^t (\omega_R + \omega_p) d\tau \right) \\ &= V_R \cos \left(\omega_R t + \frac{\Omega_P}{\omega_{\omega p}} \sin(\omega_{\omega p} t) \right) \\ v_{\omega pb} &= V_R \cos \left(\int_0^t (\omega_R + \omega_p) d\tau - \frac{2}{3}\pi \right) \\ &= V_R \cos \left(\omega_R t - \frac{2}{3}\pi + \frac{\Omega_P}{\omega_{\omega p}} \sin(\omega_{\omega p} t) \right) \end{aligned}$$

$$\begin{aligned} v_{\omega pc} &= V_R \cos \left(\int_0^t (\omega_R + \omega_p) d\tau + \frac{2}{3}\pi \right) \\ &= V_R \cos \left(\omega_R t + \frac{2}{3}\pi + \frac{\Omega_P}{\omega_{\omega p}} \sin(\omega_{\omega p} t) \right) \end{aligned} \quad (20)$$

where Ω_P is the fundamental frequency injection amplitude. $\omega_{\omega p}$ is the fundamental frequency injection radian frequency, which will be swept over a certain range.

According to the definition of $\mathbf{G}_{i\omega}$ in (9), there are two elements $G_{id\omega}$ and $G_{iq\omega}$, representing the dynamics from the excitation of fundamental frequency to its response of d - and q -output currents, respectively. Therefore, one perturbation is required at a certain frequency point $\omega_{\omega p}$ as

$$\mathbf{G}_{i\omega}(\omega_{\omega p}) = \begin{bmatrix} G_{id\omega}(\omega_{\omega p}) \\ G_{iq\omega}(\omega_{\omega p}) \end{bmatrix} = - \begin{bmatrix} i_{od}^s(\omega_{\omega p}) \\ i_{oq}^s(\omega_{\omega p}) \\ v_{\omega d}^s(\omega_{\omega p}) \\ v_{\omega q}^s(\omega_{\omega p}) \end{bmatrix}. \quad (21)$$

Since the derivation of the fundamental frequency injection $v_{\omega p abc}$ in (20) is under the assumption that the voltage amplitude of PCC voltage is unchanged, to ensure the measurement accuracy, it must be clarified that the perturbation and response signals in (19) and (21) need to be injected and measured separately. To measure \mathbf{Y}_{odq} , the dq -voltage amplitude perturbation signals v_{pd} , v_{pq} in (17) are injected. As shown in Fig. 16, after adding v_{pd} , v_{pq} to the rated dq -voltage amplitude V_R , 0 and converting to abc -frame, the reference for the three-phase controlled voltage source is obtained as v_{pabc} in (18). In this situation, the fundamental frequency of PCC voltage is not perturbed, and the phase angle θ^s for implementing transformation between dq - and abc -frames is equal to the integral of the rated fundamental frequency ω_R . Therefore, as shown in Fig. 16, the switch of θ^s is on terminal "1". To measure $\mathbf{G}_{i\omega}$, small perturbation signal ω_p is injected to the fundamental frequency of PCC

TABLE I
PARAMETERS OF DROOP-CONTROLLED INVERTER

Parameters	Value
DC voltage V_{dc}	600 V
Filter inductor L_f	3 mH
ESR of filter inductor r_{Lf}	0.08 Ω
Filter capacitor C_f	30 μ F
Distribution cable resistance R_C	0 Ω
Distribution cable inductance L_C	1 mH
ESR of distribution cable inductor r_{LC}	0.05 Ω
Cut-off frequency of power LPF ω_f	$2\pi \cdot 10$ rad/s
Rated fundamental frequency ω_0	$2\pi \cdot 50$ rad/s
Rated phase-to-phase voltage amplitude V_0	163.3 V
Active power bias P_0	1000 W
Reactive power bias Q_0	0 Var
Active power droop slope m_p	1×10^{-5} rad/(s·W)
Reactive power droop slope n_q	1×10^{-4} V/Var
Proportional gain of voltage controller k_{pv}	1
Integral gain of voltage controller k_{iv}	15
Proportional gain of current controller k_{pc}	2
Integral gain of current controller k_{ic}	0

voltage, and the voltage amplitude maintains the rated value V_R . The reference for the three-phase controlled voltage source with the perturbed fundamental frequency $v_{\omega p abc}$ is obtained as (20). In this situation, the phase angle θ^s is equal to the integral of the perturbed fundamental frequency, and the switch of θ^s is on terminal “2”. The flow chart in Fig. 16 illustrates the specific steps of measuring \mathbf{Y}_{odq} and $\mathbf{G}_{i\omega}$.

B. Measurement Results

The terminal characteristics of the droop-controlled inverter are measured with the frequency sweep approach in SABER. In accordance with Figs. 15 and 16, measurement prototypes of a single droop-controlled inverter operating in voltage and current representation are built, respectively. The parameters of the inverter control scheme and power stage are listed in Table I.

Since the small-signal dynamics are related to the steady-state operating point, to fairly compare the terminal characteristics of the same inverter in two representations, the steady-state value of circuit variables should be the same in two operation modes. The inner parameters of inverter and distribution cable are identical in two modes in accordance with Table I. Therefore, the steady-state operating points of voltage and current representations are determined by the setting value of external connected current sink and voltage source.

For the voltage operation mode, as Fig. 2 shows, the fundamental frequency ω^c and amplitude of inverter output voltage on filter capacitor $v_{C abc}$ is regulated to follow the references in (3). Since the value of droop slope is very small, the steady-state fundamental frequency and amplitude of inverter capacitor voltage are assuming to be equal to ω_0 and V_0 in Table I. Taking

the single phase as an example, Fig. 17 shows the steady-state circuit of the voltage operation mode represented in the phasor method. Once the steady-state output current is set by the current sink, the output active and reactive powers can be calculated as

$$\dot{I}_{ov} = \frac{I_R}{\sqrt{2}} \angle \varphi_{iov} \quad \dot{V}_{Cv} = \frac{V_0}{\sqrt{2}} \angle 0^\circ$$

$$\bar{S}_v = 3 \times \dot{V}_{Cv} \dot{I}_{ov}^* \quad P_v = \text{real}(\bar{S}_v) \quad Q_v = \text{imag}(\bar{S}_v) \quad (22)$$

where the subscript v denotes the operating point of voltage representation. I_R is the setting value of sink current amplitude. φ_{iov} is the phase angle of sink current. The phase angle of the inverter capacitor voltage is assumed to be 0.

For the current operation mode shown in Fig. 18, in steady state, the inverter has already completed the synchronization process with the external voltage source. Therefore, the fundamental frequency at any point of the system is clamped, which means the steady-state value of the inverter individual fundamental frequency ω^c equals to the rated fundamental frequency of external voltage source. According to the active power-frequency droop equation in (3), in order to make the steady-state output active power of current mode to be the same with that of voltage mode, the rated fundamental frequency of external voltage source ω_R should be designed as

$$\omega_R = \omega^c = \omega_0 - m_p(P_c - P_0) = \omega_0 - m_p(P_v - P_0). \quad (23)$$

Based on Fig. 18, assuming the amplitude and phase angle of external voltage source is V_R and φ_{voc} , to keep the same steady-state operating points with voltage mode, the equations of V_R and φ_{voc} can be derived as

$$\dot{V}_{oc} = \frac{V_R}{\sqrt{2}} \angle \varphi_{voc} \quad \dot{V}_{Cc} = \frac{V_0}{\sqrt{2}} \angle 0^\circ$$

$$\dot{I}_{oc} = \frac{\dot{V}_{Cc} - \dot{V}_{oc}}{Z_C}$$

$$\bar{S}_c = 3 \times \dot{V}_{Cc} \dot{I}_{oc}^*$$

$$P_c = \text{real}(\bar{S}_c) = P_v \quad Q_c = \text{imag}(\bar{S}_c) = Q_v \quad (24)$$

where the subscript c denotes the operating point of current representation.

The steady-state output active and reactive powers are designed to be equal to the bias value in Table I. Substituting $P_v = P_c = P_0$, $Q_v = Q_c = Q_0$ to (22) and (24), the calculated setting values of external connected current sink and voltage source are listed in Table II. It can be concluded that with the proper setting of external circuits, the steady-state operating points of the droop-controlled inverter in two representations can be kept the same. In simulation prototypes, the parameters of current sink in Fig. 15 and voltage source in Fig. 16 are set as Table II.

The frequency sweep range is from 0.1 to 10 000 Hz. The bode plots of measured terminal characteristics of the single

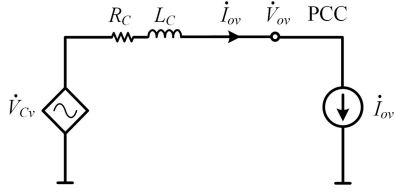


Fig. 17. Single-phase steady-state circuit of the voltage operation mode.

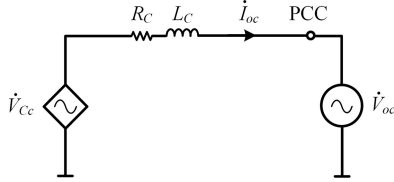


Fig. 18. Single-phase steady-state circuit of the current operation mode.

TABLE II
SETTING VALUE OF EXTERNAL CIRCUITS

Parameters	Value
Amplitude of sink current I_R	4.08 A per phase
Phase angle of sink current φ_{iov}	0
Rated fundamental frequency ω_R	$2\pi \cdot 50$ rad/s
Rated phase-to-phase voltage amplitude V_R	163.1 V
Phase angle of PCC voltage φ_{voc}	-0.008 rad

droop-controlled inverter in voltage and current representation are presented in Figs. 19 and 20, respectively.

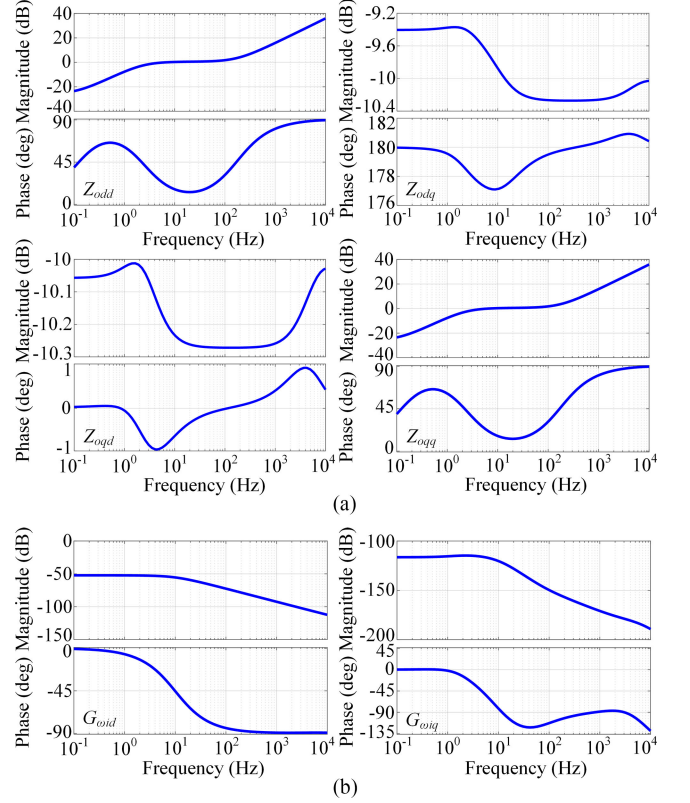
In order to verify the proposed small-signal model for the overall terminal characteristics of parallel inverters in (10), the measurement prototype of three parallel inverters is built in SABER. The parameters of each inverter are the same as those listed in Table I. Similar to single droop-controlled inverter, the overall terminal characteristics of parallel inverters can also be measured via the approaches introduced in Section IV-A. Since the overall terminal characteristics are defined in voltage representation, the shunt current injection method should be adopted. The measurement procedures are similar to those of the single droop-controlled inverter illustrated in Fig. 15.

According to (10), the overall terminal characteristics of the three parallel inverters can be calculated as

$$\begin{aligned} \mathbf{Z}_{Sodq} &= \mathbf{Z}_{odq1} \cdot \left(\mathbf{I} + \sum_{k=2}^3 \mathbf{Y}_{odqk} \cdot \mathbf{Z}_{odq1} + \sum_{k=2}^3 \mathbf{G}_{i\omega k} \cdot \mathbf{G}_{\omega i1} \right)^{-1} \\ \mathbf{G}_{S\omega i} &= \mathbf{G}_{\omega i1} \cdot \left(\mathbf{I} + \sum_{k=2}^3 \mathbf{Y}_{odqk} \cdot \mathbf{Z}_{odq1} + \sum_{k=2}^3 \mathbf{G}_{i\omega k} \cdot \mathbf{G}_{\omega i1} \right)^{-1} \end{aligned} \quad (25)$$

where the subscripts 1, 2, and 3 denote the first, the second, and the third inverter.

In order to ensure each inverter in parallel condition to maintain the same operating point as the single operation mode, the

Fig. 19. Bode plots of terminal characteristics (a) \mathbf{Z}_{odq} and (b) $\mathbf{G}_{\omega i}$ of a single droop-controlled inverter in voltage representation.

external connected current sink of three parallel inverters is set as $3 \times 4.08 = 12.24$ A per phase. In this way, the total power is 3000 W, which is equally shared by each inverter. Therefore, the terminal characteristics of each single inverter are equal to those presented in Figs. 19 and 20.

The measured overall terminal characteristics are shown in Fig. 21. Meanwhile, the calculated results based on (25) are also presented in Fig. 21. It can be observed that the calculation results coincide with the measurement results very well, which validates the proposed small-signal model for the overall terminal characteristics of parallel inverters.

V. SIMULATION VERIFICATION OF SYSTEM STABILITY PREDICTION

According to (25), the return ratio of three parallel inverters is

$$\mathbf{L} = \sum_{k=2}^3 \mathbf{Y}_{odqk} \cdot \mathbf{Z}_{odq1} + \sum_{k=2}^3 \mathbf{G}_{i\omega k} \cdot \mathbf{G}_{\omega i1}. \quad (26)$$

After measuring the terminal characteristics of each individual inverter, the characteristic loci of return ratio can be calculated to predict the stability of parallel system.

The influence of critical parameters on small-signal stability of parallel droop-controlled inverters has been investigated by conventional state-space based approaches. It suggested that the system small-signal stability is affected by active and

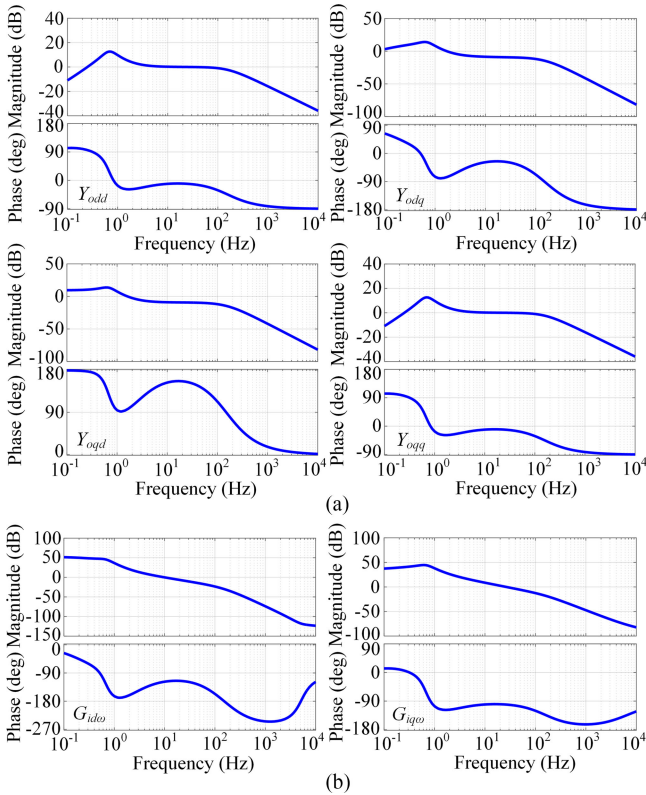


Fig. 20. Bode plots of terminal characteristics (a) Y_{odq} and (b) $G_{i\omega}$ of a single droop-controlled inverter in current representation.

reactive power droop slopes, proportional and integral gain of voltage and current controllers, as well as the network impedance [13]–[16]. Since the key issue discussed in this paper is the small-signal terminal characteristic based stability prediction approach, the impacts of these critical parameters will not be analyzed in detail due to the limited space. To prove the effectiveness of the proposed stability prediction approach, two examples with different droop slope m_p and different inductance of distribution cable L_C are studied, respectively.

A. Variation of Droop Slope m_p

Increasing the value of the active power droop slope is acknowledged to incur instability in parallel condition [13]–[16], which can find evidence in inverter terminal characteristics. As shown in Table I, the initial value of the active power droop slope m_p is 1×10^{-5} rad/(s·W). After increasing m_p by five and ten times, the measured terminal characteristics of the single inverter in voltage and current representation are presented in Figs. 22 and 23, respectively.

From Fig. 22(a), it can be observed that the impact of increasing m_p on Z_{odq} is very less. Instead, in Fig. 22(b), the amplitude of $G_{\omega id}$ and $G_{\omega iq}$ significantly increase within whole frequency range. For voltage representation, the change of active power droop slope is dominantly reflected in the proposed terminal characteristic related to fundamental frequency dynamics rather than the conventional output impedance. In Fig. 23, both Y_{odq}

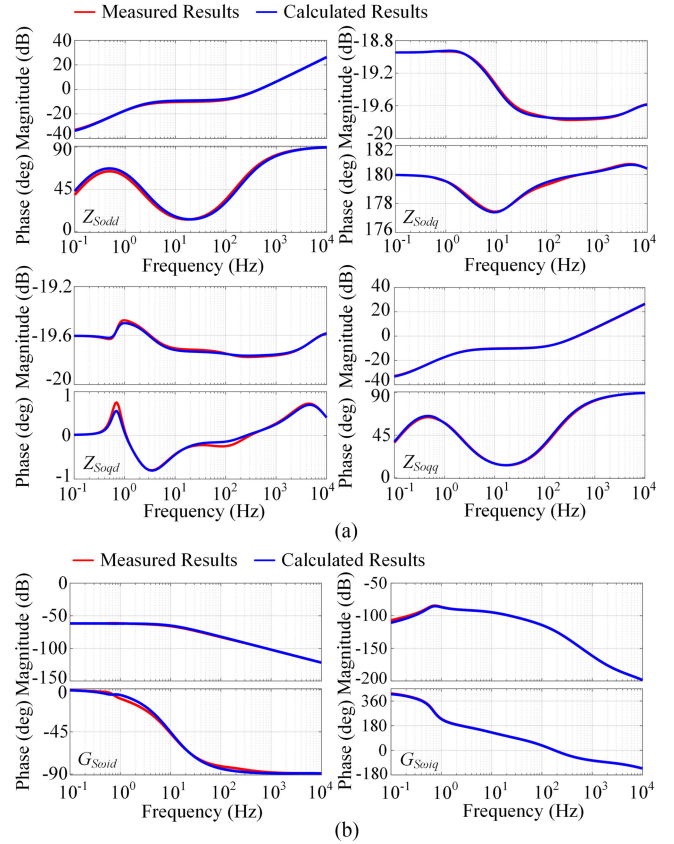


Fig. 21. Bode plots of measured and calculated overall terminal characteristics (a) Z_{Sodq} and (b) $G_{S\omega i}$ of three parallel droop-controlled inverters.

and $G_{i\omega}$ change with m_p within the low frequency range. For current representation, the change of active power droop slope reflects on both the proposed terminal characteristic and the conventional output admittance. For the bode plot of a transfer function, a RHP pole will introduce -20 dB/dec decrease in magnitude and $+90^\circ$ increase in phase. It can be observed from the bode plots in Figs. 22 and 23, the -20 dB/dec decrease in magnitude and $+90^\circ$ increase in phase never happened simultaneously, which indicates that RHP poles do not exist in Z_{odq} , $G_{\omega i}$ and Y_{odq} , $G_{i\omega}$. Therefore, a single inverter can operate stably in both voltage and current modes with three cases of m_p .

In three cases of the active droop slope, based on the terminal characteristics of each individual inverter in Figs. 22 and 23, the characteristic loci of \mathbf{L} are calculated in MATLAB. The results are plotted in Fig. 24. As discussed before in the end of Section III, the stability of parallel inverters depends on whether the characteristic loci of return ratio encircle the critical point $(-1 + j0)$ or not. In Figs. 24(a) and 24(b), the critical point $(-1 + j0)$ is not encircled by the characteristic loci of \mathbf{L} . It indicates that the parallel inverters are predicted to be stable in Case I and Case II.

When $m_{p1}=m_{p2}=m_{p3} = 1 \times 10^{-4}$ rad/(s·W), in Fig. 24(c), the characteristic loci of \mathbf{L} encircle the critical point $(-1 + j0)$ once. In Case III, the system is predicted to be unstable.

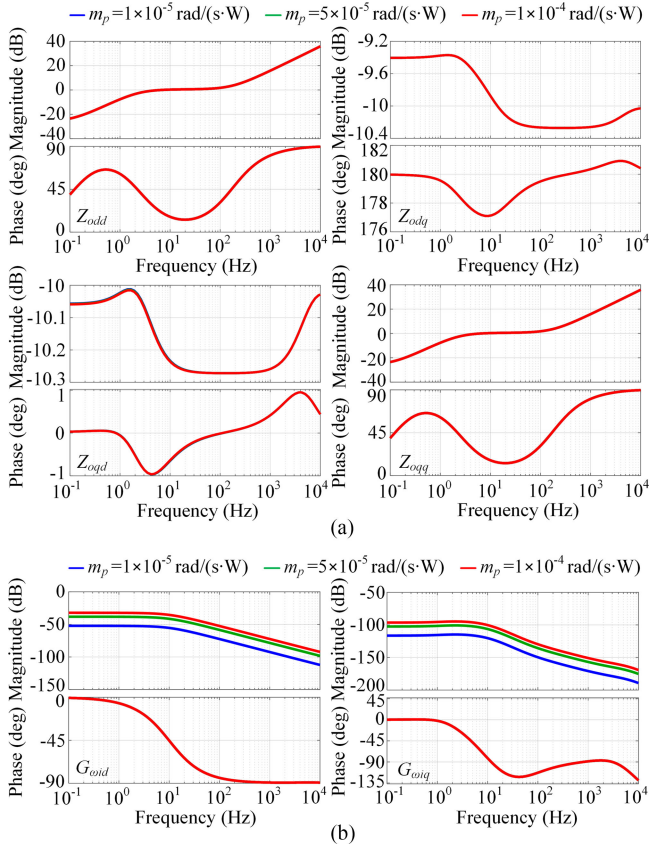


Fig. 22. Bode plots of terminal characteristics (a) Z_{odq} and (b) G_{wi} of a single inverter with three cases of m_p .

When applying GNC, the frequency at the intersection point of left-half real axis and the characteristic loci which encircled $(-1 + j0)$ is recognized as the approximate resonant frequency of the unstable system [34], [35]. The terminal characteristics of every single inverter in (26) are measured by frequency sweep approach in SABER, and then characteristic loci of the return ratio are calculated at each frequency point and connected successively in Fig. 24. Therefore, the frequency points are discrete, and the exact frequency associated to the intersection point of left-half real axis and l_1 in Fig. 24(c) cannot be obtained directly. To handle this issue, the frequency of this cross point is estimated by the frequency of two adjacent points, which is approximately equal to $(1.06 + 1.18)/2 \approx 1.1$ Hz. Since this cross point is obtained based on the small-signal model in the dq -frame, the resonant frequency in the dq -frame is predicted to be around 1.1 Hz. Eventually, the resonant frequency in the abc -frame can be predicted to be 51.1 and 48.9 Hz approximately because the rotation frequency of the dq -frame is 50 Hz [36], [37].

B. Variation of Distribution Cable Inductance L_C

When m_p is fixed as 1×10^{-4} rad/(s·W), the inductance of distribution cable L_C is changed from 1 to 3 mH ($r_{LC} = 0.08 \Omega$). For a single inverter, according to (22), the steady-

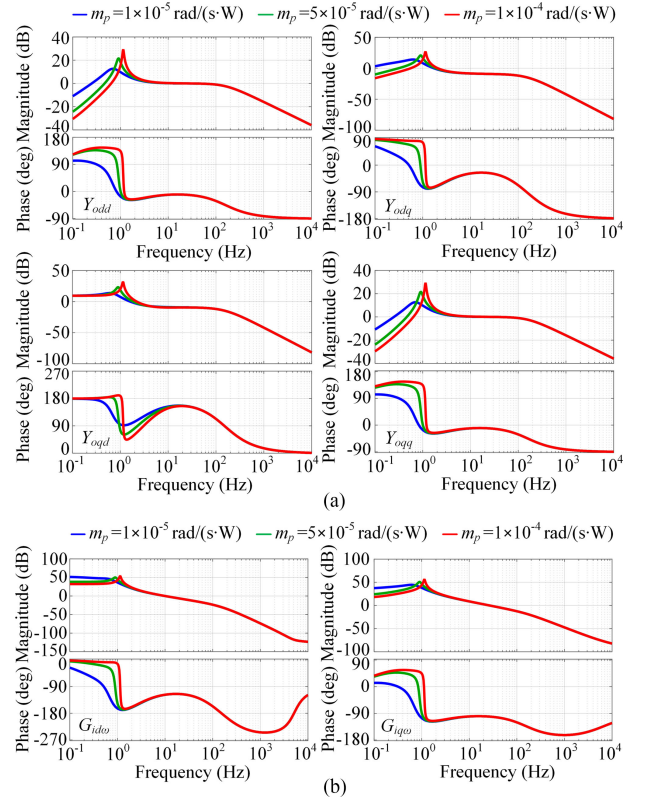


Fig. 23. Bode plots of terminal characteristics (a) Y_{odq} and (b) G_{iw} of a single inverter with three cases of m_p .

state operating point in voltage representation is unchanged. Therefore, the setting of sink current is the same as shown in Table II. In order to maintain the same steady-state operating point in current representation, based on (24), the setting of voltage amplitude and phase angle of external voltage source is change to $V_R = 163.0$ V, $\varphi_{voc} = -0.024$ rad.

The bode plots of measured terminal characteristics with distribution cable impedance $L_C = 3$ mH, $r_{LC} = 0.08 \Omega$ are presented in Figs. 25 and 26. Comparing to the terminal characteristics with $L_C = 1$ mH, $r_{LC} = 0.05 \Omega$, for voltage representation, the changing of the distribution cable impedance only reflects in Z_{odq} . Since the distribution cable is included in the model of Z_{odq} , in Fig. 25(a), the magnitude of bode plots with $L_C = 3$ mH is higher. According to Fig. 5, it can be observed that the interaction path from i_{odq}^s to ω^s is irrelevant to the distribution cable. Therefore, G_{wi} is unchanged. In Fig. 26, both Y_{odq} and G_{iw} significantly change with distribution cable impedance. According to the definition of terminal characteristics in current representation, the amplitude and phase angle differences between inverter capacitor voltage and PCC voltage determine the inverter output current via the distribution cable. Therefore, its impedance affects the interaction dynamics from both ω^s and v_{odq}^s to i_{odq}^s . The -20 dB/dec decrease in magnitude and $+90^\circ$ increase in phase are not exhibited in the bode plots in Figs. 25 and 26, which suggests that the single inverter can operate stably in both voltage and current modes with $m_p = 1 \times 10^{-4}$ rad/(s·W), $L_C = 3$ mH.

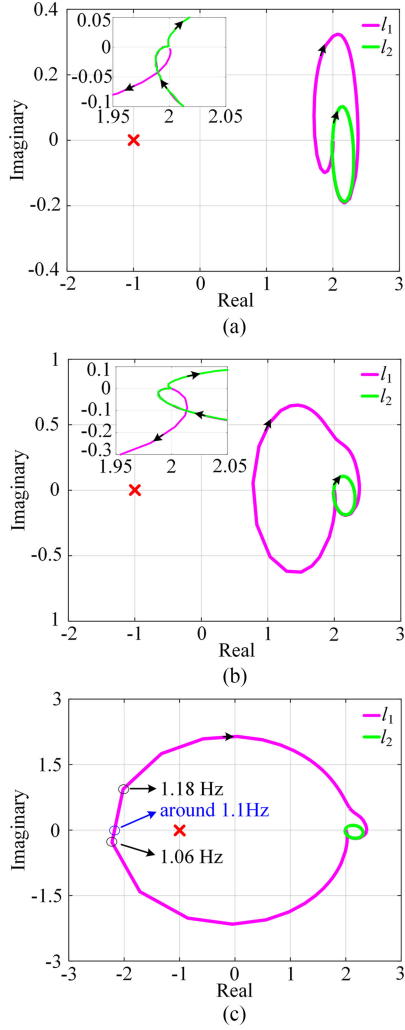


Fig. 24. Characteristic loci of the system return ratio in three cases. (a) Case I: $m_{p1} = m_{p2} = m_{p3} = 1 \times 10^{-5} \text{ rad}/(\text{s} \cdot \text{W})$. (b) Case II: $m_{p1} = m_{p2} = m_{p3} = 5 \times 10^{-5} \text{ rad}/(\text{s} \cdot \text{W})$. (c) Case III: $m_{p1} = m_{p2} = m_{p3} = 1 \times 10^{-4} \text{ rad}/(\text{s} \cdot \text{W})$.

When $m_{p1} = m_{p2} = m_{p3} = 1 \times 10^{-4} \text{ rad}/(\text{s} \cdot \text{W})$, $L_{C1} = L_{C2} = L_{C3} = 3 \text{ mH}$, based on the terminal characteristics of individual inverters in Figs. 25 and 26, the characteristic loci of the return ratio in (26) are calculated in MATLAB and plotted in Fig. 27. The critical point $(-1+j0)$ is not encircled, which suggests that the parallel three inverters operate stably in this condition. Comparing to Fig. 24(c) where $L_{C1} = L_{C2} = L_{C3} = 1 \text{ mH}$, larger distribution cable impedance contributes to damping the resonance between parallel inverters and improve system stability.

VI. EXPERIMENTAL VERIFICATION

The basic principle to verify the effectiveness of the proposed approach is comparing the stability prediction results with the time-domain waveforms. In this section, time-domain experimental results are presented to validate the terminal characteristic-based stability prediction in Section V.

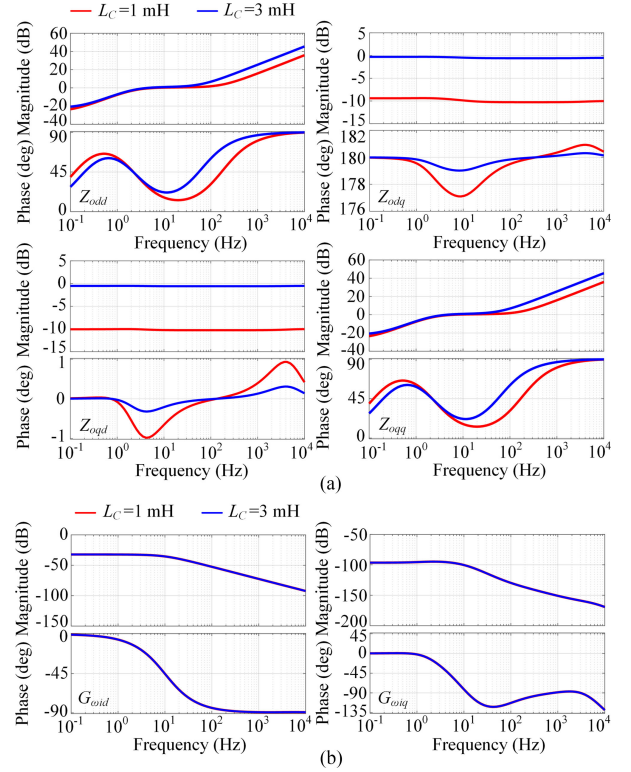


Fig. 25. Bode plots of terminal characteristics (a) Z_{odq} and (b) G_{ω_i} of a single inverter with different distribution cable impedance.

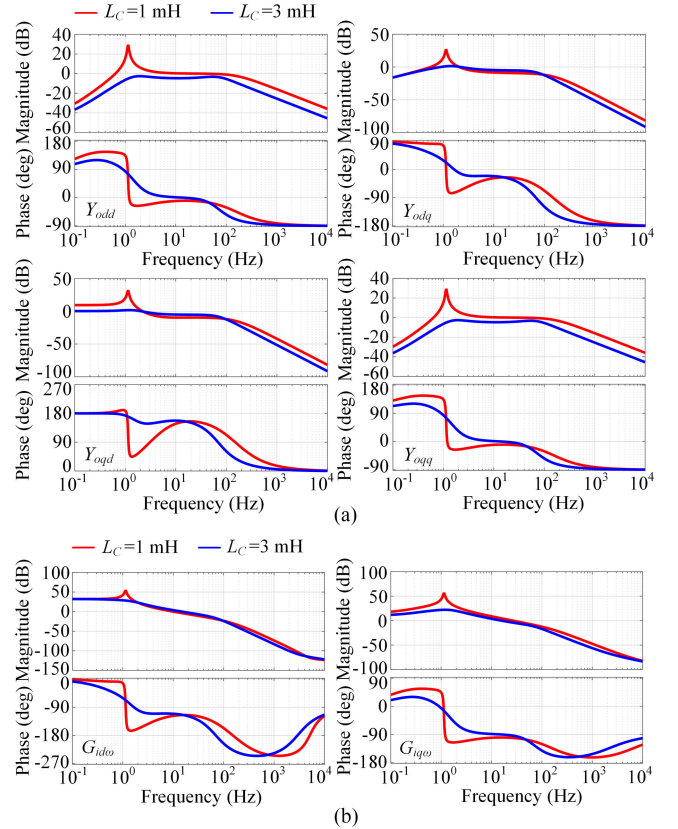


Fig. 26. Bode plots of terminal characteristics (a) Y_{odq} and (b) $G_{i\omega}$ of a single inverter with different distribution cable impedance.

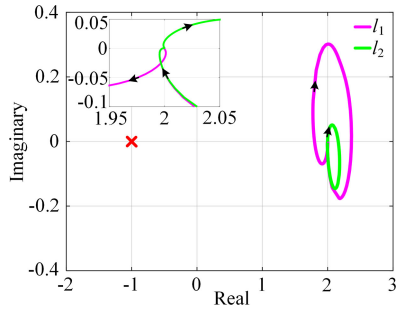


Fig. 27. Characteristic loci of system return ratio with $m_{p1} = m_{p2} = m_{p3} = 1 \times 10^{-4}$ rad/(s · W) and $L_{C1} = L_{C2} = L_{C3} = 3$ mH.



Fig. 28. Hardware platform of parallel inverters: (a) overall view and (b) inside view of each inverter.

The experiments are conducted on a hardware platform shown in Fig. 28. This platform consists of four parallel inverters, three-phase loads, and one grid simulator, which can test and perform various working conditions of parallel inverters and ac microgrids. The inner structure of each inverter is shown in Fig. 28(b). The first layer includes a three-phase inverter unit MWINV-9R144, control board, and I/O board. At the second layer, a programmable dc source feeds to the dc side of the inverter, providing 600 V dc voltage. The three-phase LC filter is adopted to filter the switching ripples. The inverter is connected to the ac bus through the solid state relay and distribution cable impedance in the third layer. The power stage and control scheme of each inverter in the hardware platform is the same with Fig. 1. In experiments, Inv 1, Inv 2, and Inv 3 are operated. The parameters of these three inverters are identical, in accordance with Table I. The three-phase programmable electronic load Chroma 63804 working in a constant current mode is adopted as the current sink in the voltage operation mode, whereas the grid simulator Chroma 61860 acts as the external voltage source in the current operation mode.

A. Variation of Droop Slope m_p

First, the inductance of the distribution cable L_C is 1 mH. With three cases of the active power droop slope m_p , a single droop-controlled inverter is operated in voltage and current modes, respectively. The parameter setting of the external electronic load and grid simulator follows Table II. The experimental waveforms are shown in Figs. 29 and 30. For each operating state, the waveforms of 10 s are presented. It can be observed

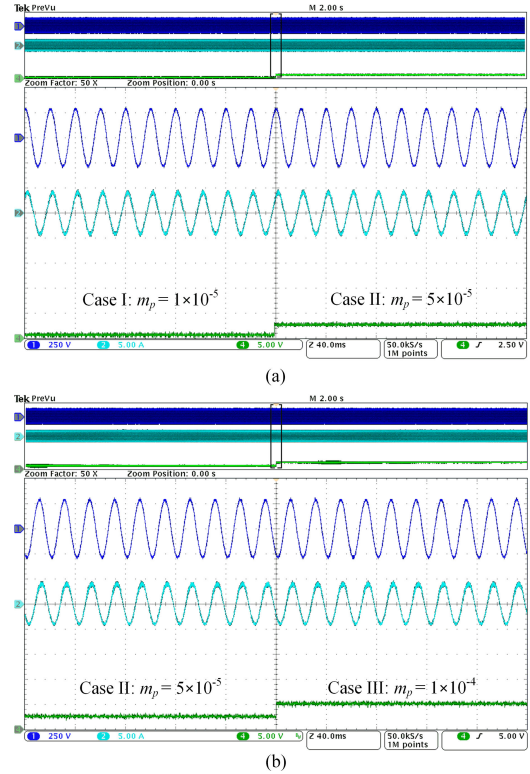


Fig. 29. Experimental waveforms of a single inverter in the voltage operation mode with three cases of active power droop slope m_p : CH1, line-to-line PCC voltage, v_{PCCab} , 250 V/div; CH2, output current, i_{oa} , 5 A/div; CH4, active power droop slope, m_p , 10^{-4} rad/(s·W)/div.

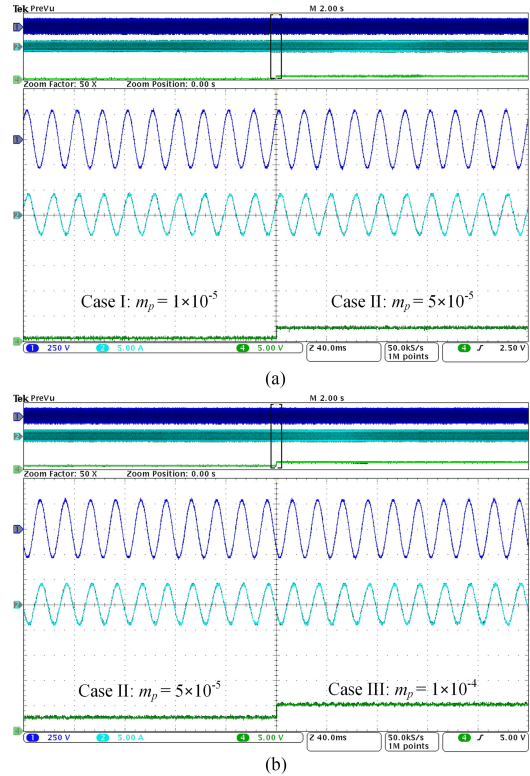


Fig. 30. Experimental waveforms of a single inverter in the current operation mode with three cases of active power droop slope m_p : CH1, line-to-line PCC voltage, v_{PCCab} , 250 V/div; CH2, output current, i_{oa} , 5 A/div; CH4, active power droop slope, m_p , 10^{-4} rad/(s·W)/div.

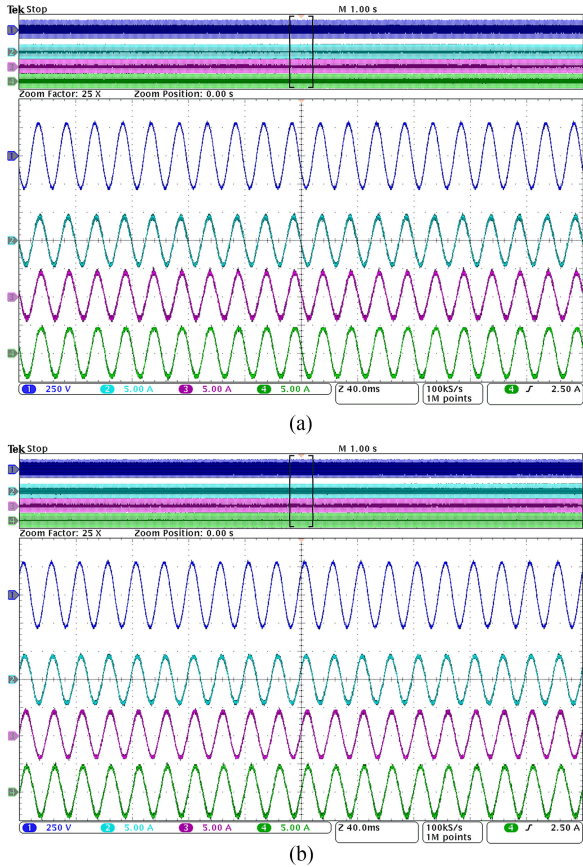


Fig. 31. Experimental waveforms of parallel Inv 1, Inv 2, and Inv 3 in (a) Case I: $m_{p1} = m_{p2} = m_{p3} = 1 \times 10^{-5} \text{ rad}/(\text{s} \cdot \text{W})$; (b) Case II: $m_{p1} = m_{p2} = m_{p3} = 5 \times 10^{-5} \text{ rad}/(\text{s} \cdot \text{W})$: CH1, line-to-line PCC voltage, v_{PCCab} , 250 V/div; CH2, Inv 1 output current, i_{oa1} , 5 A/div; CH3, Inv 2 output current, i_{oa2} , 5 A/div; CH4, Inv 3 output current, i_{oa3} , 5 A/div.

that a single inverter can be operated stably with three cases of m_p in both voltage and current modes.

Second, three inverters are paralleled together, connecting to the electronic load with the sink current of 12.24 A per phase. With first two cases of $m_{p1}/m_{p2}/m_{p3}$, the waveforms of PCC voltage and output current of three inverters are shown in Fig. 31. The experimental waveforms suggest that the parallel three inverters operate stably in Case I and Case II, which coincides with the prediction results in Figs. 24(a) and 24(b).

With $m_{p1} = m_{p2} = m_{p3} = 1 \times 10^{-4} \text{ rad}/(\text{s} \cdot \text{W})$, the experimental waveforms are shown in Fig. 32. It suggests that the parallel three inverters lose stability in Case III, which validates the prediction result in Fig. 24(c). The waveform data in Fig. 32 are processed by MATLAB to conduct the fast Fourier transform (FFT) analysis. The results are shown in Fig. 33. It can be observed from Fig. 32 that the distortion of PCC voltage is much smaller than that of output current of three inverters, which is also revealed by the FFT analysis results in Fig. 33. Since the resonance behaves as the power exchange between parallel inverters, the total harmonic distortion of inverter output current is relatively higher. The PCC voltage and inverter output current all show two main resonant components

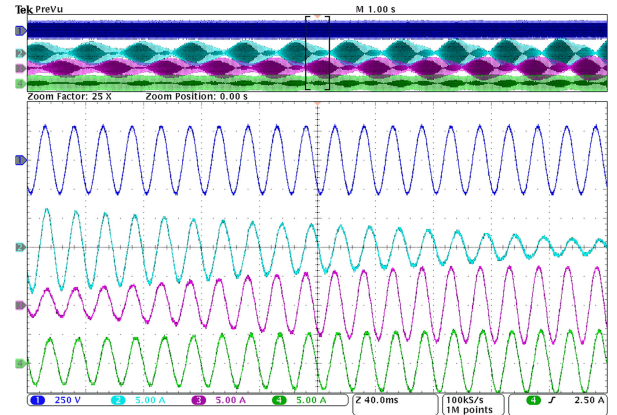


Fig. 32. Experimental waveforms of parallel Inv 1, Inv 2, and Inv 3 in Case III: $m_{p1} = m_{p2} = m_{p3} = 1 \times 10^{-4} \text{ rad}/(\text{s} \cdot \text{W})$: CH1, line-to-line PCC voltage, v_{PCCab} , 250 V/div; CH2, Inv 1 output current, i_{oa1} , 5 A/div; CH3, Inv 2 output current, i_{oa2} , 5 A/div; CH4, Inv 3 output current, i_{oa3} , 5 A/div.

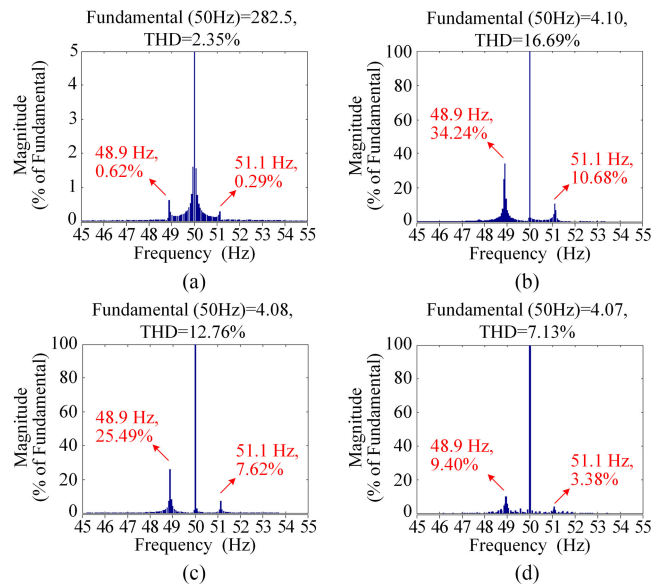


Fig. 33. FFT analysis results of experimental waveforms in unstable case. (a) CH1, line-to-line PCC voltage, v_{PCCab} ; (b) CH2, Inv 1 output current, i_{oa1} ; (c) CH3, Inv 2 output current, i_{oa2} ; (d) CH4, Inv 3 output current, i_{oa3} .

at 48.9 and 51.1 Hz, which coincides with the prediction in Fig. 24(c) and further proves the accuracy of the proposed small-signal terminal characteristic model and stability prediction approach.

B. Variation of Distribution Cable Inductance L_C

In this section, the droop slope m_p is fixed as $1 \times 10^{-4} \text{ rad}/(\text{s} \cdot \text{W})$, and the distribution cable inductance L_C is changed from 1 to 3 mH. The waveforms of a single inverter operating in voltage and current modes are presented in Fig. 34. When $m_{p1} = m_{p2} = m_{p3} = 1 \times 10^{-4} \text{ rad}/(\text{s} \cdot \text{W})$, $L_{C1} = L_{C2} = L_{C3} = 3 \text{ mH}$, the waveforms of three parallel inverters are shown in Fig. 35. In accordance with

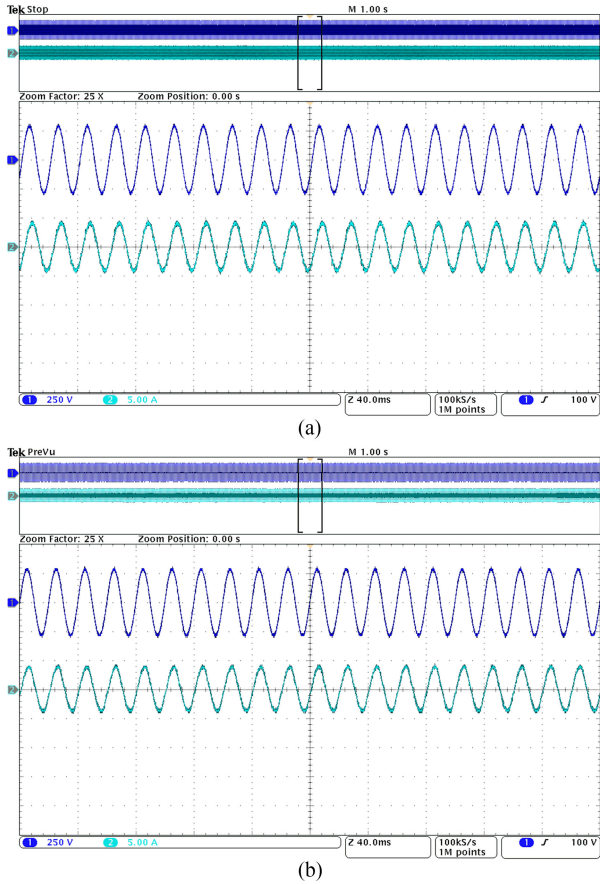


Fig. 34. Experimental waveforms of single inverter with $m_p = 1 \times 10^{-4} \text{ rad}/(\text{s} \cdot \text{W})$ and $L_C = 3 \text{ mH}$. (a) Voltage operation mode. (b) Current operation mode: CH1 line-to-line PCC voltage, v_{PCCab} , 250 V/div; CH2, output current, i_{oa} , 5 A/div.

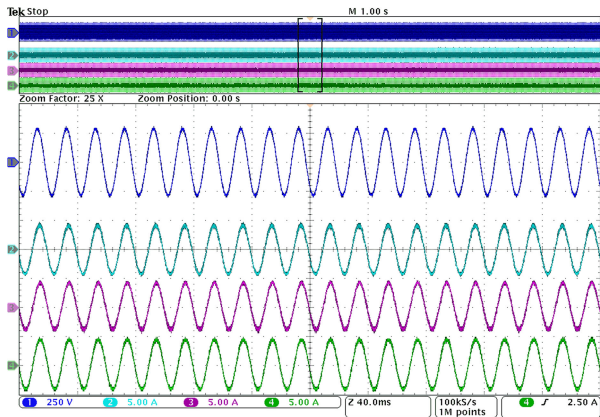


Fig. 35. Experimental waveforms of parallel Inv 1, Inv 2, and Inv 3 with $m_{p1} = m_{p2} = m_{p3} = 1 \times 10^{-4} \text{ rad}/(\text{s} \cdot \text{W})$, $L_{C1} = L_{C2} = L_{C3} = 3 \text{ mH}$: CH1 line-to-line PCC voltage, v_{PCCab} , 250 V/div; CH2, Inv 1 output current, i_{oa1} , 5 A/div; CH3, Inv 2 output current, i_{oa2} , 5 A/div; CH4, Inv 3 output current, i_{oa3} , 5 A/div.

the stability prediction result in Fig. 27, after increasing L_C to 3 mH, the parallel system could maintain a stable operation with $m_{p1} = m_{p2} = m_{p3} = 1 \times 10^{-4} \text{ rad}/(\text{s} \cdot \text{W})$.

VII. CONCLUSION

This paper presents a novel set of small-signal terminal characteristics for the droop-controlled inverter to characterize its fundamental frequency dynamics. Then, a terminal characteristic-based stability prediction approach is proposed for parallel droop-controlled inverters. Besides conventional impedance and admittance, an additional term associated with the proposed terminal characteristics is added in the system return ratio to cover the fundamental frequency interactions between parallel droop-controlled inverters. In different operating conditions, experimental results suggest that the proposed approach can provide accurate prediction of system stability. This paper characterizes the dynamic interactions between parallel droop-controlled inverters based on the comprehensive terminal characteristics of individual inverters, which provides an approach for small-signal stability analysis of ac microgrids.

REFERENCES

- [1] R. H. Lasseter, "Certs microgrid," in *Proc. IEEE Int. Conf. Syst. Syst. Eng.*, San Antonio, TX, USA, 2007, pp. 1–5.
- [2] N. Hatziaargyriou, H. Asano, R. Iravani, and C. Marnay, "Microgrids," *IEEE Power Energy Mag.*, vol. 5, no. 4, pp. 78–94, Jul. 2007.
- [3] B. Kroposki, C. Pink, R. DeBlasio, H. Thomas, M. Simões, and P. K. Sen, "Benefits of power electronic interfaces for distributed energy systems," *IEEE Trans. Energy Convers.*, vol. 25, no. 3, pp. 901–908, Sep. 2010.
- [4] J. Rocabert, A. Luna, F. Blaabjerg and P. Rodríguez, "Control of power converters in ac microgrids," *IEEE Trans. Power Electron.*, vol. 27, no.11, pp. 4734–4749, Nov. 2012.
- [5] M. C. Chandorkar, D. M. Divan, and R. Adapa, "Control of parallel connected inverters in standalone AC supply systems," *IEEE Trans. Ind. Appl.*, vol. 29, no. 1, pp. 136–143, Jan./Feb. 1993.
- [6] J. M. Guerrero, L. García de Vicuña, J. Matas, M. Castilla, and J. Miret, "A wireless controller to enhance dynamic performance of parallel inverters in distributed generation systems," *IEEE Trans. Power Electron.*, vol. 19, no. 5, pp. 1205–1213, Sep. 2004.
- [7] J. He, Y. W. Li, J. M. Guerrero, F. Blaabjerg, and J. C. Vasquez, "An islanding microgrid power sharing approach using enhanced virtual impedance control scheme," *IEEE Trans. Power Electron.*, vol. 28, no. 11, pp. 5272–5282, Nov. 2013.
- [8] F. Cingoz, A. Elrayyah, and Y. Sozer, "Plug-and-play nonlinear droop construction scheme to optimize islanded microgrid operations," *IEEE Trans. Power Electron.*, vol. 32, no. 4, pp. 2743–2756, Apr. 2017.
- [9] J. M. Guerrero, J. C. Vasquez, J. Matas, L. G. de Vicuña, and M. Castilla, "Hierarchical control of droop-controlled ac and dc microgrids – A general approach toward standardization," *IEEE Trans. Ind. Electron.*, vol. 58, no. 1, pp. 158–172, Jan. 2011.
- [10] Q. C. Zhong and Y. Zeng, "Universal droop control of inverters with different types of output impedance," *IEEE Access*, vol. 4, pp. 702–712, Feb. 2016.
- [11] Y. Yang, S. S. Ho, S. C. Tan, and S. Y. R. Hui, "Small-signal model and stability of electric springs in power grids," *IEEE Trans. Smart Grid*, vol. 9, no. 2, pp. 857–865, Mar. 2018.
- [12] L. Zhang, L. Harnefors, and H. Nee, "Power-synchronization control of grid-connected voltage-source converters," *IEEE Trans. Power Syst.*, vol. 25, no. 2, pp. 809–820, May 2010.
- [13] E. Coelho, P. Cortizo, and P. Garcia, "Small-signal stability for parallel connected inverters in stand-alone AC supply systems," *IEEE Trans. Ind. Appl.*, vol. 38, no.2, pp. 533–542, Mar./Apr. 2002.
- [14] Y. Mohamed and E. El-Saadany, "Adaptive decentralized droop controller to preserve power sharing stability of paralleled inverters in distributed generation microgrids," *IEEE Trans. Power Electron.*, vol. 23, no. 6, pp. 2806–2816, Nov. 2008.
- [15] N. Pogaku, M. Prodanovic, and T. C. Green, "Modeling, analysis and testing of autonomous operation of an inverter-based microgrid," *IEEE Trans. Power Electron.*, vol. 22, no. 2, pp. 613–625, Mar. 2007.
- [16] K. Yu, Q. Ai, S. Wang, J. Ni, and T. Lv, "Analysis and optimization of droop controller for microgrid system based on small-signal dynamic model," *IEEE Trans. Smart Grid*, vol. 7, no. 2, pp. 695–705, Mar. 2016.

- [17] S. Hiti, V. Vlatkovic, D. Boroyevich, and F. C. Lee, "A new control algorithm for three-phase PWM buck rectifier with input displacement factor compensation," *IEEE Trans. Power Electron.*, vol. 9, no. 2, pp. 173–180, Mar. 1994.
- [18] S. Chandrasekaran, D. Boroyevich, and D. K. Lindner, "Input filter interaction in three phase ac-dc converters," in *Proc. 30th IEEE Power Electron. Spec. Conf.*, Charleston, SC, USA, 1999, pp. 987–992.
- [19] A. MacFarlane and I. Postlethwaite, "The generalized Nyquist stability criterion and multivariable root loci," *Int. J. Control*, vol. 25, no. 1, pp. 81–127, Feb. 1977.
- [20] M. Belkhat, "Stability criteria for ac power systems with regulated loads," *Ph.D. dissertation*, Purdue Univ., West Lafayette, IN, USA, Dec. 1997.
- [21] J. Huang, K. A. Corzine, and M. Belkhat, "Small-signal impedance measurement of power-electronics-based AC power systems using line-to-line current injection," *IEEE Trans. Power Electron.*, vol. 24, no. 2, pp. 445–455, Feb. 2009.
- [22] V. Valdivia, A. L'azar, A. Barrado, P. Zumel, C. Fern'andez, and M. Sanz, "Impedance identification procedure of three-phase balanced voltage source inverters based on transient response measurements," *IEEE Trans. Power Electron.*, vol. 26, no. 12, pp. 3810–3816, Dec. 2011.
- [23] G. Francis, R. Burgos, D. Boroyevich, F. Wang, and K. Karimi, "An algorithm and implementation system for measuring impedance in the D-Q domain" in *Proc. 3rd IEEE Energy Convers. Congr. Expo.*, Phoenix, AZ, USA, 2011, pp. 3221–3228.
- [24] X. Wang, F. Blaabjerg, M. Liserre, Z. Chen, J. He, and Y. Li, "An active damper for stabilizing power-electronics-based ac systems," *IEEE Trans. Power Electron.*, vol. 29, no. 7, pp. 3318–3329, Jul. 2014.
- [25] X. Wang, L. Harnefors, and F. Blaabjerg, "Unified impedance model of grid-connected voltage-source converters," *IEEE Trans. Power Electron.*, vol. 33, no. 2, pp. 1775–1787, Feb. 2018.
- [26] B. Wen, D. Boroyevich, R. Burgos, P. Mattavelli, and Z. Shen, "Analysis of D-Q small-signal impedance of grid-tied inverters," *IEEE Trans. Power Electron.*, vol. 31, no. 1, pp. 675–687, Jan. 2016.
- [27] B. Wen, D. Dong, D. Boroyevich, R. Burgos, P. Mattavelli, and Z. Shen, "Small-signal stability analysis of three-phase ac systems in the presence of constant power loads based on measured d-q frame impedances," *IEEE Trans. Power Electron.*, vol. 30, no. 10, pp. 26–38, Oct. 2015.
- [28] Z. Liu, J. Liu, W. Bao, and Y. Zhao, "Infinity-norm of impedance-based stability criterion for three-phase ac distributed power systems with constant power loads," *IEEE Trans. Power Electron.*, vol. 30, no. 6, pp. 3030–3043, Jun. 2015.
- [29] Z. Liu, J. Liu, X. Hou, Q. Dou, and T. Liu, "Output impedance modeling and stability prediction of three-phase paralleled inverters with master-slave sharing scheme based on terminal characteristics of individual inverters," *IEEE Trans. Power Electron.*, vol. 31, no. 7, pp. 5306–5320, Jul. 2016.
- [30] J. M. Guerrero, V. Luis Garcia de, J. Matas, M. Castilla, and J. Miret, "Output impedance design of parallel-connected UPS inverters with wireless load-sharing control," *IEEE Trans. Power Electron.*, vol. 52, no. 4, pp. 1126–1135, Aug. 2005.
- [31] M. Mao, Y. Ding, Y. Shen, and L. Chang, "Hybrid impedance-based modelling and stability analysis of IMG-PICDPS," in *Proc. 9th IEEE Energy Convers. Congr. Expo.*, Cincinnati, OH, USA, 2017, pp. 3353–3358.
- [32] M. A. Azzouz and E. F. E. Saadany, "Multivariable DG impedance modeling for the microgrid stability assessment," in *Proc. IEEE Int. Symp. Circuits Syst.*, Montreal, QC, Canada, 2016, pp. 1642–1645.
- [33] S.-K. Chung, "A phase tracking system for three phase utility interface inverters," *IEEE Trans. Power Electron.*, vol. 15, no. 3, pp. 431–438, May 2000.
- [34] Y. Song and F. Blaabjerg, "Overview of DFIG-based wind power system resonances under weak networks," *IEEE Trans. Power Electron.*, vol. 32, no. 6, pp. 4370–4394, Jun. 2017.
- [35] D. Lu, X. Wang, and F. Blaabjerg, "Impedance-based analysis of dc-link voltage dynamics in voltage-source converters," *IEEE Trans. Power Electron.*, vol. 34, no. 4, pp. 3973–3985, Apr. 2019.
- [36] L. Harnefors, "Modeling of three-phase dynamic systems using complex transfer functions and transfer matrices," *IEEE Trans. Ind. Electron.*, vol. 54, no. 4, pp. 2239–2248, Aug. 2007.
- [37] J. Shen, S. Schröder, H. Stage, and R. W. De Doncker, "Precise modeling and analysis of DQ-frame current controller for high power converters with low pulse ratio," in *Proc. Energy Convers. Congr. Expo.*, 2012, pp. 61–68.



Shike Wang (S'15) received the B.S. degree in electrical engineering from Xi'an Jiaotong University, Xi'an, China, in 2014. She is currently working toward the Ph.D. degree with Xi'an Jiaotong University.

Her research interests include coordinative control of parallel inverters, small-signal modeling, and stability of three-phase ac microgrids.



Zeng Liu (S'09–M'14) received the B.S. degree from Hunan University, Changsha, China, and the M.S. and Ph.D. degrees from Xi'an Jiaotong University (XJTU), Xi'an, China, in 2006, 2009, and 2013, respectively, all in electrical engineering.

He then joined XJTU as a Faculty Member of electrical engineering, where he is currently an Associate Professor. From 2015 to 2017, he was with the Center for Power Electronics Systems, Virginia Polytechnic Institute and State University, Blacksburg, VA, USA, as a Visiting Scholar. His research

interests include modeling and control of parallel inverters as well as grid-tied converters, and small-signal stability of three-phase ac power electronics systems.

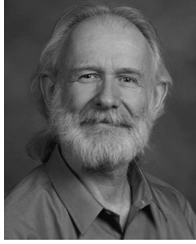


Jinjun Liu (M'97–SM'10–F'19) received the B.S. and Ph.D. degrees in electrical engineering from Xi'an Jiaotong University (XJTU), Xi'an, China, in 1992 and 1997, respectively.

He then joined the XJTU Electrical Engineering School as a faculty. From late 1999 to early 2002, he was with the Center for Power Electronics Systems, Virginia Polytechnic Institute and State University, Blacksburg, VA, USA, as a Visiting Scholar. In late 2002, he was promoted to a Full Professor and then the Head of the Power Electronics and Renewable

Energy Center, XJTU, which now comprises of 17 faculty members and more than 100 graduate students and carries one of the leading power electronics programs in China. From 2005 to early 2010, he served as an Associate Dean of Electrical Engineering School, XJTU, and from 2009 to early 2015, the Dean for Undergraduate Education of XJTU. He is currently a XJTU Distinguished Professor of Power Electronics, sponsored by Chang Jiang Scholars Program of Chinese Ministry of Education. He coauthored three books (including one textbook), published more than 400 technical papers in peer-reviewed journals and conference proceedings, holds nearly 50 invention patents (China/US), and delivered for many times plenary keynote speeches and tutorials at IEEE conferences or China national conferences in power electronics area. His research interests include power quality control and utility applications of power electronics, microgrids for sustainable energy and distributed generation, and more/all electronic power systems.

Dr. Liu received for eight times governmental awards at national level or provincial/ministerial level for scientific research/teaching achievements. He also received the 2006 Delta Scholar Award, the 2014 Chang Jiang Scholar Award, the 2014 Outstanding Sci-Tech Worker of the Nation Award, and the IEEE Transactions on Power Electronics 2016 Prize Paper Award. He served as the IEEE Power Electronics Society (PELS) Region 10 Liaison and then China Liaison for ten years, an Associate Editor for the IEEE TRANSACTIONS ON POWER ELECTRONICS for 12 years, and since 2015, the Vice President for Membership of IEEE PEELS. He is on the Board of China Electrotechnical Society and was elected the Vice President of the CES PEELS in 2013. Since 2013, he has been the Vice President for International Affairs, China Power Supply Society and since 2016, the inaugural Editor-in-Chief of *CPSS Transactions on Power Electronics and Applications*. Since 2013, he has been serving as the Vice Chair of the Chinese National Steering Committee for College Electric Power Engineering Programs.



Dushan Boroyevich (S'81–M'86–SM'03–F'06) received the Dipl.Ing. degree from the University of Belgrade, Belgrade, Serbia, in 1976, and the M.S. degree from the University of Novi Sad, Novi Sad, Serbia, in 1982. He received the Ph.D. degree in 1986 from Virginia Polytechnic Institute and State University (Virginia Tech), Blacksburg, VA, USA.

From 1986 to 1990, he was an Assistant Professor and Director of the Power and Industrial Electronics Research Program with the Institute for Power and Electronic Engineering, University of Novi Sad. He then joined the Bradley Department of Electrical and Computer Engineering, Virginia Tech, as an Associate Professor. He is currently the University Distinguished Professor with the Department and Director of the Center for Power Electronics Systems. His research interests include electronic energy systems, multiphase power conversion, power electronics systems modeling and control, and integrated design of power converters.

Dr. Boroyevich was the President of the IEEE Power Electronics Society for 2011–2012. He is a member of the US National Academy of Engineering and is a recipient of numerous awards, including the IEEE William E. Newell Power Electronics Technical Field Award and the European Power Electronics Association Outstanding Achievement Award.



Rolando Burgos (S'96–M'03) received the B.S. degree in electronics engineering, the Electronics Engineering Professional degree, and the M.S. and Ph.D. degrees in electrical engineering from the University of Concepción, Chile, in 1995, 1997, 1999, and 2002, respectively.

In 2002, he joined, as a Postdoctoral Fellow at the Center for Power Electronics Systems (CPES), Virginia Polytechnic Institute and State University (Virginia Tech), Blacksburg, VA, USA, becoming a Research Scientist in 2003, and a Research Assistant Professor in 2005. In 2009, he joined ABB Corporate Research, Raleigh, NC, USA, where he was a Scientist (2009–2010) and a Principal Scientist (2010–2012). In 2010, he was appointed as an Adjunct Associate Professor with the Department of Electrical and Computer Engineering, North Carolina State University at the Future Renewable Electric Energy Delivery and Management Systems Center. In 2012, he returned to Virginia Tech where he is currently an Associate Professor with The Bradley Department of Electrical and Computer Engineering, CPES faculty, and member of the CPES Executive Board. His research interests include the modeling and control of power electronics converters and systems, wide-bandgap semiconductor-based power conversion, packaging and integration, electromagnetic interference and electromagnetic compatibility, multiphase multilevel power converters, grid power electronics systems, and stability of ac and dc power systems.

Dr. Burgos is member of the IEEE Power Electronics Society where he currently serves the Chair of the Technical Committee on Power and Control Core Technologies. He also serves as an Associate Editor of the IEEE TRANSACTIONS ON POWER ELECTRONICS, and the IEEE JOURNAL OF EMERGING AND SELECTED TOPICS IN POWER ELECTRONICS. He is a member of the IEEE Industry Applications Society, the IEEE Industrial Electronics Society, and the IEEE Power and Energy Society.